University of Alberta

PLANAR PHOTONIC CRYSTALS FOR BIOSENSING AND NONLINEAR POLYMER INTEGRATION

by

Steven C. Buswell 

A thesis submitted to the Faculty of Graduate Studies and Research in partial fulfillment of the requirements for the degree of **Master of Science**

Department of Electrical and Computer Engineering

Edmonton, Alberta
Spring 2008

Your file Votre référence
ISBN: 978-0-494-45786-3
Our file Notre référence
ISBN: 978-0-494-45786-3

Abstract

Photonic crystals are periodic nanostructures offering unique potential for the manipulation of light. This work investigates the fabrication of planar silicon photonic crystals, photonic crystal waveguides, photonic crystal waveguide biosensors, and the incorporation of nonlinear ISAM films in silicon photonic crystal structures. Silicon photonic crystals were fabricated using a combination of high resolution electron beam lithography and dry etching. Photonic crystal waveguide biosensors were realized with a bulk sensitivity of 88 nm/RIU. A 5.6 nm thick MPMTS film was detected with a 3.2 nm mode cut-off shift. Specific detection of streptavidin was demonstrated with a 0.86 nm mode cut-off shift. An improved design was realized and shown to have a bulk sensitivity of 120 nm/RIU, a 40% improvement. A hybrid fabrication approach to incorporating nonlinear self-assembled polymers with a silicon photonic crystal was also developed. Here the evanescent field of a photonic crystal guided mode interacts with the nonlinear polymer.

To my parents, who taught me how to learn, and never told me to stop.

Acknowledgements

I feel privileged to have been given an amazing opportunity to study with some of the world's best people and facilities. My research and this thesis would not have been possible without the assistance that so many have generously offered. I would like to offer special thanks to my supervisor Dr. Stéphane Evoy who provided me with the opportunity undertake this work. Dr. Evoy has consistently offered his full support, providing guidance and encouragement, as well as ensuring that I had the resources I needed to perform to my potential. I would also like to gratefully acknowledge my other supervisor Dr. Vien Van, whose assistance with optical matters was instrumental to the project. In particular, I would like to thank Dr. Van for his help with setting up a photonic characterization lab and for many engaging discussions, from which I learned a great deal.

From the beginning my partner Aruna Kroetch has been of great assistance. As a nanofabrication beginner, I greatly benefitted from the accelerated learning process which Aruna was able to guide me through. Throughout this project Aruna has been my first source for advice and first source of comfort when things went wrong. I would also like to give thanks to my adopted lab-mate, Ashok Prabhu, with whom I was able to talk through many problems and who graciously indulged my interest in peripherally relevant thought exercises.

This research would never have been possible without the assistance of my collaborators. For the ISAM-related portions of this work I would like to offer my thanks to Vladimir Kochergin and Roger Duncan of Luna Innovations Inc. Both Vladimir and Roger made significant contributions in guiding the course of this work. My thanks go in particular to Vladimir for ensuring that my trip to Blacksburg was a success. I would also like to acknowledge my collaborators at Virginia Tech, Cemil Durak and Dr. Randy Heflin, who

graciously supplied some of their ISAM films for my work. Thanks also to Dr. Vincent Wright of Dr. Buriak's group, without whose chemistry skills, the biofunctionalization experiments would never have been possible.

In the course of this project, I spent seemingly countless hours in the University of Alberta's Nanofab. The staff of the Fab is primarily responsible for making it an enjoyable place to work. In particular, I would like to thank Kristian Olsen, Keith Franklin, Scott Munro, Les Schowalter, and Stephanie Bozic for their role in training, fixing, and helping. Thanks also to Peng Li and Mirwais Atkary for electron beam lithography help, to Miro Belov for insight into the Cryo process, and to Daniel Salomon at the National Institute for Nanotechnology for his assistance with scanning electron microscopy.

Finally I would like to thank all my fellow students in Dr. Evoy's lab, Dr. Van's lab, and elsewhere for their assistance and friendship. Having good lab-mates made coming in each day that much easier.

Table of Contents

List of Figures

List of Abbreviations

1D	one-dimensional
2D	two-dimensional
3D	three-dimensional
BAW	bulk acoustic wave
BESOI	bonded and etched back silicon on insulator
BSA	bovine serum albumin
CMOS	complementary metal oxide semiconductor
CROW	coupled resonant oscillator waveguide
CPU	central processing unit
DMSO	dimethyl sulfoxide
DNA	deoxyribonucleic acid
EBL	electron beam lithography
FDTD	finite difference time domain
FBMS	fixed beam moving stage
GLAD	glancing angle deposition
ICP	inductively coupled plasma
IPA	isopropanol
IR	Infrared
ISAM	ionically self-assembled monolayer

LOD	limit of detection
MEMS	microelectromechanical systems
MIBK	methyl isobutyl ketone
MOS	metal oxide semiconductor
MPTMS	3-mercaptopropyltrimethoxysilane
MZI	Mach-Zehnder interferometer
PAH	poly(allylamine hydrochloride)
PBS	phosphate buffered saline
PC	photonic crystal
PCBS	poly1-[4-(3-carboxy-4-hydroxyphenylazo) bensensulfonamido]-1,2-ethanediyl, sodium salt
PCF	photonic crystal fiber
PCW	photonic crystal waveguide
PMMA	polymethyl methacrylate
PPC	planar photonic crystal
PWE	plane-wave expansion
QCM	quartz crystal microbalance
RIE	reactive ion etch
RIU	refractive index unit
RF	radio frequency
SAW	surface acoustic wave
SEM	scanning electron micrograph

SIMOX	separation by implantation of oxygen
SOI	silicon-on-insulator
SPR	surface plasmon resonance
TE	transverse electric
TIR	total internal reflection
TM	transverse magnetic

1 Photonic Crystals

1.1 Introduction to photonic crystals

Photonic crystals are periodic nanostructures that do not support electromagnetic propagation in certain frequency ranges. Their potential to manipulate light on a subwavelength scale has generated considerable interest. While generally regarded as artificially engineered materials, photonic crystals also appear naturally as opals and in the wings of some butterflies and moths [1,2].

Photonic crystals (PCs) are defined by a wavelength scale periodic modulation of their dielectric constant and are typically classified by the dimensionality of this periodicity (Figure 1.1). One-dimensional photonic crystals are well known as Bragg reflectors and have been extensively studied for application in waveguiding [3], vertical cavity surface emitting lasers [4], and for improving the extraction efficiency of light emitting diodes [5]. Two-dimensional photonic crystals expand their periodicity to two dimensions. Photonic crystal fibers [6] are an example, where light confined by the photonic bandgap propagates along the invariant direction. Likewise, fully three dimensional photonic crystals maintain periodicity in all directions.

While the third dimension of a 2D PC is generally assumed to be invariant, this is not always the case. Planar photonic crystals (PPC) compose a class of structures where the photonic crystal medium is confined to a thin region in the third dimension by total internal reflection.

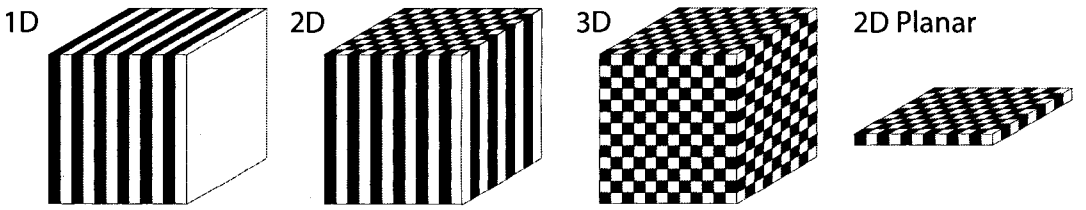

Figure 1.1: Schematic of a photonic crystal with 1-dimensional, 2-dimensional, and 3-dimensional periodicity.

Two-dimensional planar photonic crystals (PPCs), created by perforating a dielectric slab, have received considerable attention [7]. The primary advantage of PPC structures is that they can be fabricated using techniques developed for creating planar microelectronic circuitry. This allows for lithographic tunability such that the central frequency of the bandgap can be varied in patterning. In this manner, an array of PPC lasers with different lasing wavelengths could, for example, be integrated onto a uniform substrate [8].

The one dimensional photonic bandgap effect was first investigated in 1887 by Lord Rayleigh [9]. It was not until 1987 that this effect was generalized to multiple dimensions, as a mechanism for inhibiting spontaneous emission [10] and for photon localization [11]. Several years following, the first 3D full bandgap photonic crystal was demonstrated in the microwave regime by careful machining of metal [12]. The first demonstration of a two-dimensional photonic crystal operating in the infrared regime appeared in 1995 [13] and was created in porous silicon. Photonic crystals with bandgaps in the near-IR and visible regime soon followed. Significant effort has been since spent to create 3D photonic crystal structures using techniques such as self-assembly, glancing angle deposition (GLAD), top-down fabrication, and multiple thin-film deposition. Fabrication of 3D PCs remains difficult, however.

1.2 The photonic bandgap

The photonic bandgap concept is analogous to the electronic bandgap observed in semiconductor materials, where a regular arrangement of atoms results in a periodic electric potential. Likewise, the periodicity of the dielectric material creates a photonic bandgap. For a homogenous material, the wave dispersion relation can be expressed as:

$$w = k\frac{c}{n} \tag{1.1}$$

where ω is the frequency, k is the propagation constant, c is the speed of light in vacuum, and n is the refractive index of the material. With reference to a periodic medium, equation 1.1 is usually expressed equivalently as a function of the periodic length, a:

$$\frac{wa}{2\pi c} = \frac{a}{\lambda_0} = \frac{1}{2n}.\frac{ka}{\pi} \tag{1.2}$$

Considering the refractive index to be a periodic function modifies the dispersion, such that the relationship between frequency and wavelength becomes non-linear, opening a frequency gap at the Brillouin zone boundary where no corresponding wavevector exists (Figure 1.2). The origin of this gap can be understood by considering the behaviour at the Brillouin zone boundary. At this point, a standing wave is formed with the wavelength of light being twice the period of the dielectric modulation. This wave can be decomposed as a sine function and a cosine function. One of these modes will tend to be confined primarily in the high index material, while the other mode will be primarily confined in the low index material. The bandgap arises from the field energy difference between these two modes.

There are numerous approaches to creating a periodic modulation of the refractive index. Since the bandgap should exist for all propagation directions, it is helpful to maintain high rotational symmetry. This reduces the mismatch between bandgaps for different propagation directions. The most common 2D photonic crystal symmetries are the square and hexagonal lattices, which have two-fold and three-fold rotational symmetry respectively. Quasi-crystals with higher order symmetry have also been demonstrated [14, 15] but remain exotic.

As with electronic bandgaps, a sufficient understanding can be gained from the study of propagation only along the high symmetry points [16]. For a hexagonal lattice photonic crystal, these high symmetry directions are Γ-M, Γ-K, M-K (Figure 1.3).

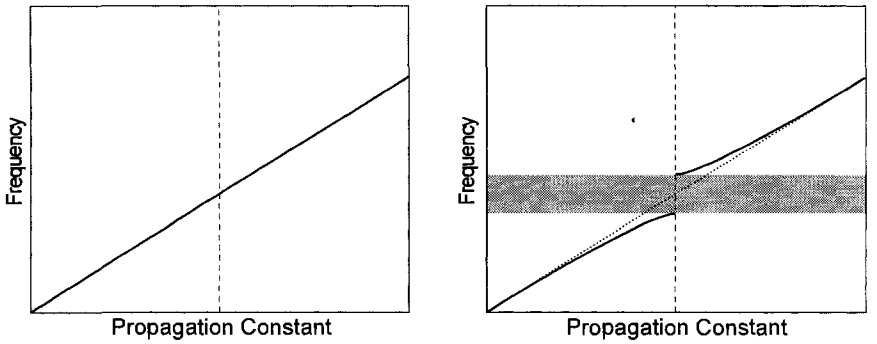

Figure 1.2: Comparison of free-space dispersion (left) with dispersion in a periodic medium (right). In a periodic medium the band bends as it approaches the Brillouin zone boundary (dashed). The shaded region represents the bandgap which is created.

The dispersion diagram for a hexagonal 2D photonic crystal of air holes with radius 0.35a in silicon is illustrated in Figure 1.4. A full bandgap exists for the TE polarization but does not for TM polarization. While it is possible for a photonic crystal to possess a bandgap for both TE and TM polarizations, it is not generally the case.

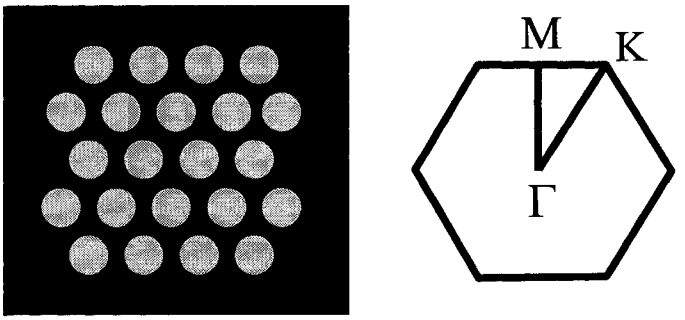

Figure 1.3: Schematic layout of a hexagonal lattice photonic crystal (left) and its corresponding wavevector space plot, indicating high symmetry points (right).

The photonic bandgap is defined relative to the crystal lattice dimension, a. Being scale independent, the band gap can be shifted to any position on the electromagnetic spectrum by scaling the lattice. The precise width and center wavelength of the photonic bandgap is

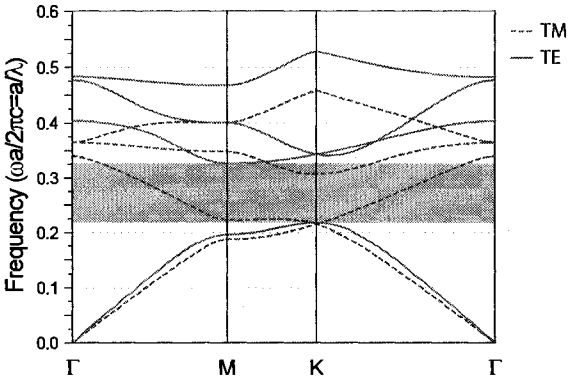

Figure 1.4: Photonic band diagram for a 2D hexagonal-lattice photonic crystal with air hole of radius 0.35a in silicon computed by plane wave expansion. This structure supports a TE bandgap but no TM bandgap. The shaded region shows the range of frequencies for which there is a full bandgap.

determined by a number of factors including the lattice dimension, the refractive index of the 'high-index' material, the refractive index of the 'low-index' material, the fraction of high and low index materials, as well as the symmetry and geometry of the structure. For instance, Figure 1.5 illustrates how the center frequency and width of the bandgap of a 2D hexagonal lattice photonic crystal of air holes in silicon is shifted by modifying the hole size. The TE bandgap moves to higher frequencies and widens with increasing hole size, reaching a peak width for a radius of 0.42a, then shrinks to a close.

1.3 Photonic crystal modelling techniques

Effective modelling is of critical importance to the design of complex devices leveraging the unique properties of photonic crystals. Modelling is typically concerned with predicting the band structure, waveguide dispersion curves, and with the spectral response to an external wave source. To simplify what can become intensive computations, three dimensional structures are often modeled as simpler two-dimensional structures, with an effective index determined by the 3D guided mode. The technique does not account for the dispersion of the guided mode, so the accuracy decreases with increasing slab index contrast. For instance, the 'effective-index' method has been shown to generate an error of 5-10% over a 100 nm bandwidth of an SOI waveguide structure [17].

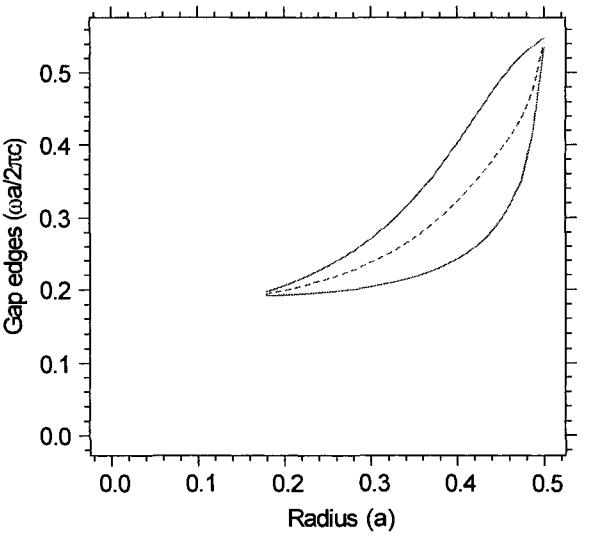

Figure 1.5: Variation of the TE photonic band gap as a function of hole radius for a 2D air-hole silicon hexagonal-lattice photonic crystal as computed with the plane wave expansion technique.

While a number of modelling methods have been proposed, the plane-wave expansion method and the finite difference time domain (FDTD) method remain the most common techniques and have been employed in this work.

1.3.1 Plane-wave expansion

The plane-wave expansion (PWE) technique is a frequency domain method for solving the eigenmodes of a structure. Maxwell's equations for an inhomogenous dielectric medium without charges or currents are given by:

$$\nabla \times E = -\frac{\partial B}{\partial t} \tag{1.3}$$

$$\nabla \times H = \frac{\partial D}{\partial t} \tag{1.4}$$

$$\nabla \cdot D = 0 \tag{1.5}$$

$$\nabla \cdot B = 0. \tag{1.6}$$

Assuming the fields have a harmonic time dependence and that the magnetic permeability μ is equal to μ_0, the curl equations become:

$$\nabla \times E = -j\omega\mu_{\circ}H(r) \tag{1.7}$$

$$\nabla \times H = j\omega\epsilon(r)\epsilon_{\circ}E(r) \tag{1.8}$$

which can then be combined in terms of the magnetic field, yielding:

$$\nabla \times \left(\frac{1}{\epsilon(r)}\nabla \times H(r)\right) = \frac{\omega^2}{c^2}H(r). \tag{1.9}$$

One can then define a Hermitian operator (Equation 1.10) with eigenfunctions that are therefore complete and orthogonal [18]:

$$\Theta = \nabla \times \frac{1}{\epsilon(r)}\nabla \times . \tag{1.10}$$

Since the permittivity ϵ_r is periodic, Bloch's theorem allows the expansion of the magnetic field H_r and the electric field E_r as a set of plane-waves. By plotting the frequency versus plane-wave wavevectors, we can construct the dispersion relation for a photonic crystal. A significant advantage of the plane-wave expansion technique is that the field only needs to be solved over one basis cell of a periodic structure. The PWE technique does not, however, provide any information about losses. In particular it does not reveal leaky modes, even when their associated loss is minimal.

Plane-wave expansion simulations reported here have been computed using the RSoft BandSolve package.

1.3.2 FDTD

The finite-difference time-domain (FDTD) method was first introduced by Yee in 1966 [19] and remains a popular technique for modelling electromagnetics in many applications. The FDTD method directly solves Maxwell's equations in the time domain by discretizing time and space into a number of nodes, and by replacing Maxwell's differential equations with finite difference equations. For each incremental step, the field is computed by relating each node to its neighbors using the difference equations subject to any boundary or initial conditions.

The FDTD method can be used to model both wave propagation and as well the band structure of a system. Unlike plane wave expansion simulations, FDTD provides information regarding loss. The principal disadvantage to FDTD is that it is computationally demanding, making three dimensional simulations particularly challenging.

Finite difference simulations presented here have been performed using a simulation code written by Dr. Vien Van from the University of Alberta's department of Electrical and Computer Engineering.

1.4 Planar photonic crystals

Though the theoretical treatment of 2D photonic crystals is reasonably straightforward, it is difficult to fabricate an effectively infinitely deep photonic crystal. Planar photonic crystals (PPCs) present an alternative [20]. Planar photonic crystals are 2-dimensional photonic crystals with a finite vertical extent (Figure 1.6). They confine light in the out-of-plane direction through the refractive index contrast of the dielectric heterostructure. The thickness of the slab is generally such that it is optically thin, supporting only the fundamental mode. Slabs based on III-V semiconductors have been reported [21] and widely used for the design of active structures, whereas silicon (SOI) is mostly used for passive devices.

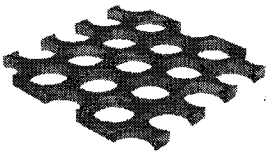

Figure 1.6: Planar photonic crystal with hexagonally arranged low index (air) holes in a high index (silicon) slab.

A 2D photonic crystal may have an out-of-plane extent which cannot be considered to be optically thick. The bandgap becomes increasingly sensitive to changes of the slab thickness as the slab becomes thinner (Figure 1.7) Higher order modes will eventually be supported within the slab as it becomes thicker, disrupting the bandgap [22].

One consequence of the finite slab thickness is that it is possible for photons to leak to radiating modes when their incident angle is greater than the critical angle for total internal reflection. As such, radiation becomes a source of loss in the photonic crystal structure. These lossy regions can be visualized by superimposing the dispersion of the slab's cladding materials onto the band diagram for the photonic crystal. Figure 1.8 illustrates the case of a silicon photonic crystal which can leak to air and oxide cladding layers depicted by the light lines overlaid onto the photonic band diagram. Photonic crystal modes located above these 'light-lines' will radiate away from slab. As would be intuitively expected, the photonic band gap only exists for modes which are guided within the slab. 3D plane wave simulations do not reveal useful information about bands located above the light cone (Figure 1.9).

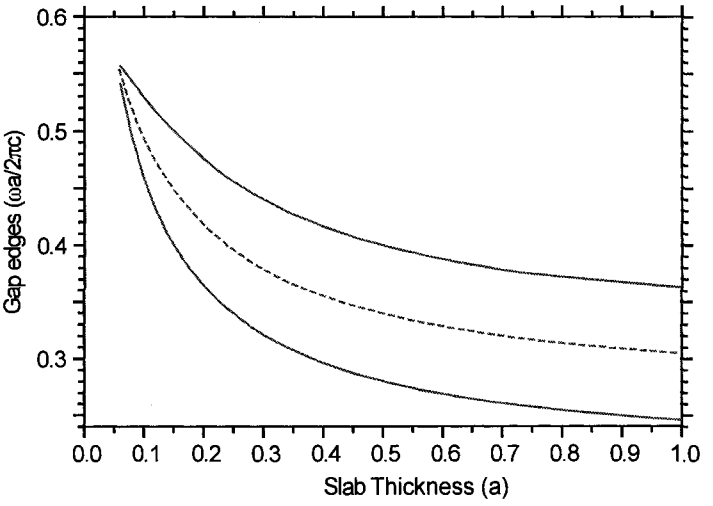

Figure 1.7: Variation of the bandgap edges for a hexagonal photonic crystal slab of 0.35a radius air holes in silicon. As the silicon slab becomes thinner, the bandgap narrows and rises to higher frequency.

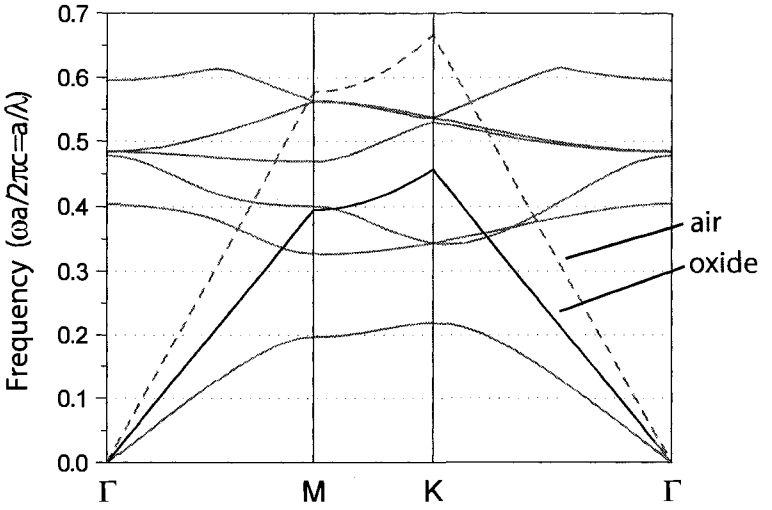

Figure 1.8: Band diagram (TE) for a 2D hexagonal silicon photonic crystal. The dispersion of the cladding materials is overlaid as the solid black line (oxide light-line) and the dashed gray line (air light-line).

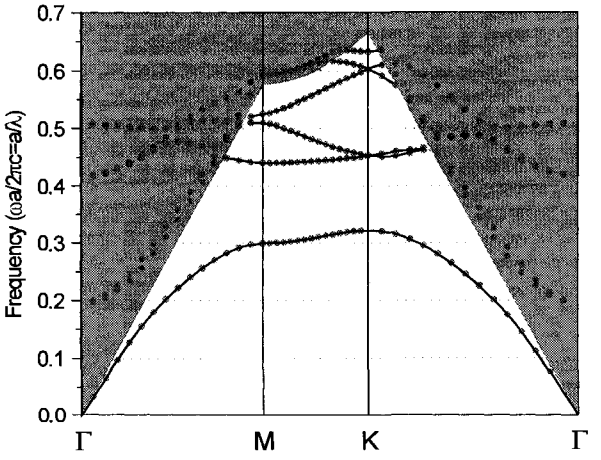

Figure 1.9: Band diagram (TE) for an air-clad 3D hexagonal silicon photonic crystal with hole radius 0.35a and thickness 0.3a. Shaded regions indicate a continuum of states.

1.5 Summary

Photonic crystals are structures featuring a periodic modulation of their refractive index, which opens a band of frequencies with no corresponding wavevector. Frequencies inside this bandgap are not supported within the photonic crystal. The design of photonic crystals relies upon electromagnetic simulations computed with FDTD or PWE methods. Planar photonic crystals have emerged as a promising platform that allows multidimensional control of light via the photonic bandgap effect combined with TIR. Their planar nature makes them ideally suited for fabrication using established microfabrication techniques.

2

Planar 2D Photonic Crystal Waveguides

2.1 Introduction

Silicon wire waveguides use a high refractive index to tightly confine light and have been demonstrated to have low loss and good suitability for integrated optics. The photonic crystal waveguide (PCW) is a novel kind of waveguide that confines light by distributed Bragg reflection from a dielectric lattice.

By introducing a defect into a photonic crystal, a corresponding defect state is introduced into the bandgap such that the defect site supports a localized field. In further analogy to semiconductor physics, removing these holes is akin to adding donor defects to the crystal, pulling down states from the valence band [23]. A series of defects created in this manner will couple to each other such that a propagating wave is supported. Provided the band is beneath the light cone, energy can thereby propagate along the line defect without loss. While it may be possible for the photonic crystal waveguide structure to support waveguiding by total internal reflection (TIR) (most 'photonic crystal' fibers operate in this manner), photonic bandgap guidance is a distinct effect.

There was considerable initial excitement regarding the potential for creating PCWs with extremely sharp bends and low-loss [24, 25]. However, the losses associated with silicon

photonic crystal waveguides and bends remains relatively high. In their present state, PCWs are typically employed as specialized components, with the task of guiding light given to more traditional strip waveguides. An exciting aspect of photonic crystal waveguides is their potential for engineered dispersion [26]. By combining nonlinear material with these dispersion properties it also becomes possible to enhance nonlinear effects [27].

2.2 Photonic crystal waveguide varieties

The optical waveguide is an important component of all integrated optical systems, acting in a similar capacity to a wire in electrical systems. Photonic crystal waveguides can be realized in a number of ways (Figure 2.1). Coupled resonator optical waveguides (CROW) are formed by creating a string of resonant cavities which couple to each other. Line defect waveguides can be created by removing a single row of holes (W1 waveguide) or with the removal of multiple rows of holes (W2, W3, etc.).

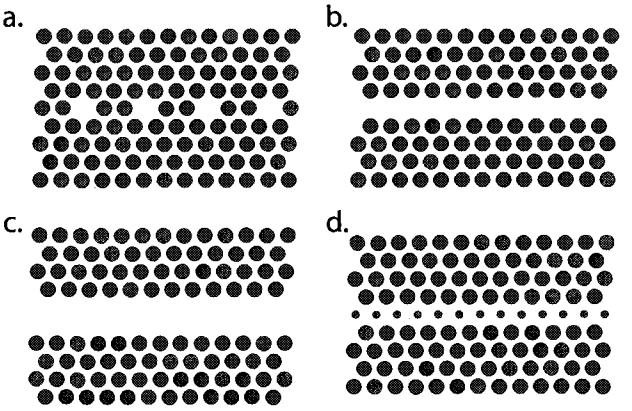

Figure 2.1: Photonic crystal waveguides of four types: (a) CROW guide, (b) W1 waveguide, (c) W2 waveguide, and (d) line defect waveguide created by shrinking a row of holes.

By far the most reported variety is the W1 photonic crystal waveguide, first proposed by Meade et al. in 1994 [28]. Removing a row of holes is straightforward and does not require more strenuous fabrication tolerances than would be required to create the bulk photonic crystal. The characteristic projected band diagram of the W1 waveguide is seen in Figure 2.2. By operating near the mode cut-off of the even mode, single-mode propagation

is ensured. Removing multiple rows of holes increases the population of bands inside the bandgap making single mode operation more difficult to acheive.

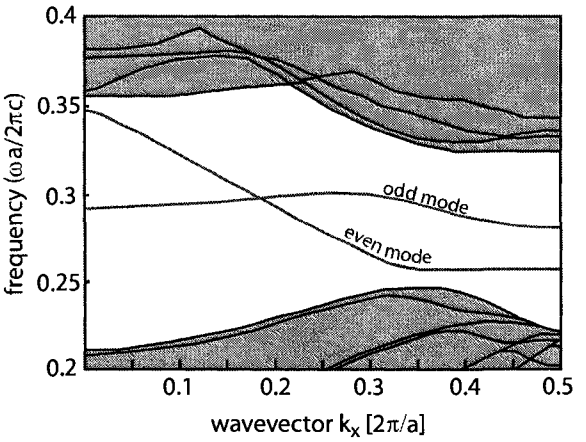

Figure 2.2: Projected band diagram for a W1 photonic crystal waveguide in silicon with 0.35a holes. 2D plane wave simulation using the effective-index method. Simulation courtesy of Ashok Prabhu.

Defect sites can be created by modifying the photonic crystal lattice in other ways too. Rather than removing the holes entirely, a waveguide of the same concept as the W1 can be created by shrinking (or enlarging) a row of holes. Shrinking the low-index holes tends to pull states down from the air band, while enlarging holes tends to pull states up from the dielectric band.

2.3 Modelling photonic crystal waveguides

The band structure of photonic crystal waveguides can be modelled using the plane wave expansion method, similar to bulk photonic crystals. Rather than simulating a single unit cell, a 'super-cell' (Figure 2.3) containing the defect is defined as the basis of the structure. The simulation results will therefore be representative of an infinite set of waveguides. The waveguides can, however, be assumed to be non-interacting given that they are sufficiently separated.

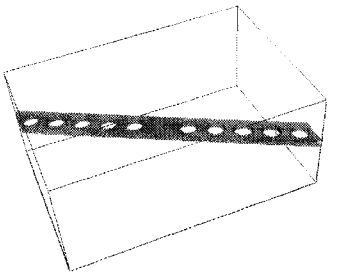

Figure 2.3: A supercell equi-index surface for a three dimensional W1 photonic crystal waveguide. This cell forms the periodic basis of a photonic crystal waveguide planewave expansion simulation.

Figure 2.4 presents the TE-like dispersion diagram projected in the direction of propagation for an air-clad photonic crystal waveguide with hole radius of 0.35a fabricated in a silicon slab of thickness 0.73a. The darkly shaded regions correspond to modes which are supported by the photonic crystal slab and the lightly shaded region corresponds to the continuum of modes which radiate away from the slab. There are several photonic crystal waveguide bands supported by the line defect within the bandgap.

Considering a photonic crystal slab asymmetrically clad with oxide and air, the result is similar (Figure 2.5). Because of the oxide cladding, the light-line descends, obscuring the higher frequency modes. As well, TE and TM modes cannot be separated when the vertical symmetry is broken, but TE-like and TM-like modes can still be identified by comparison to symmetric simulations.

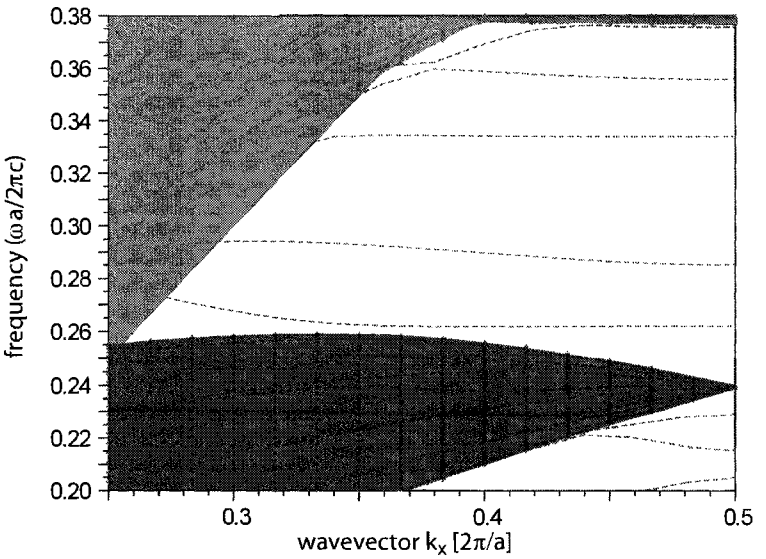

Figure 2.4: TE band diagram projected in the propagation direction for a 3D air-clad hexagonal lattice silicon photonic crystal waveguide. Shaded regions consist of a continuum of states either guided by the photonic crystal slab or radiating above the light line. Several photonic crystal waveguide modes are visible.

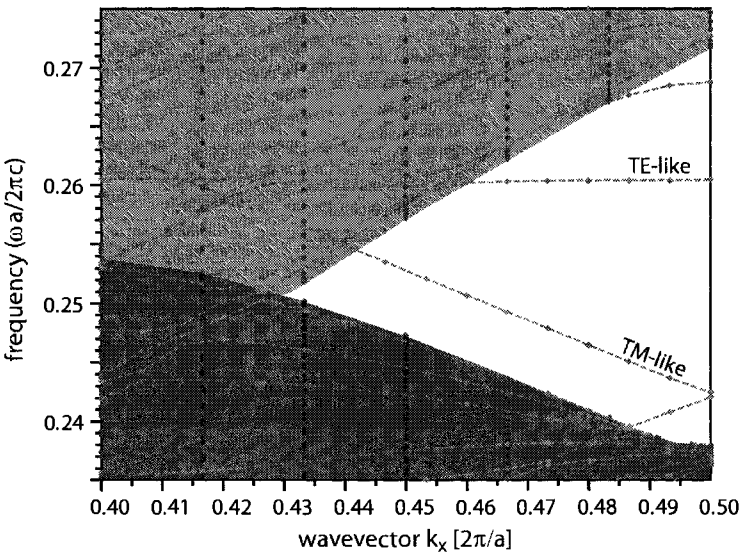

Figure 2.5: Band diagram projected in the propagation direction for a 3D hexagonal lattice silicon photonic crystal waveguide clad asymmetrically with air and oxide. The TE and TM modes cannot be strictly separated, though TE-like and TM-like modes can still be indentified.

2.4 Summary

Photonic crystal waveguides can be formed by introducing a series of coupled defects in the crystal. The W1 'line-defect' waveguide remains the most common variety of photonic crystal waveguide and is created by removing a rows of holes. Photonic crystal waveguides can be modelled similarly to photonic crystals by choosing a periodic basis cell incorporating the defect state. Simulations predict a region of single mode operation near the mode cut-off for the lowest frequency W1 photonic crystal waveguide.

3

Fabrication of Silicon Photonic Crystals

3.1 Introduction

The lattice of a silicon photonic crystal having an infrared bandgap is on the order of 400 nm, with the inter-hole spacing nearing 100 nm. Such feature size renders their fabrication somewhat challenging. Photonic crystals rely on distributed reflection, which makes them very sensitive to roughness and defects, even when it is far below wavelength scale. This chapter details the fabrication procedure developed in the University of Alberta Nanofab for the realization of planar photonic crystals in silicon-on-insulator (SOI) wafers.

3.2 Silicon-on-insulator as a material system

Silicon possesses notable advantages as a nanophotonic material. It is widely available, transparent in the infrared region, has established microfabrication techniques, and has a high refractive index lending itself to high optical confinement. An SOI wafer, seen in cross-section in Figure 3.1, is composed of three layers, a thin single crystal silicon layer above an oxide layer which in turn rests upon a silicon handle. The refractive index heterostructure created by the silicon film bounded by oxide on one side and air on the other confines the light to the silicon slab by total internal reflection.

Silicon on insulator wafers can be readily purchased with a single crystal silicon layer thickness of tens to a few hundred nanometers and with a buffer-oxide layer thickness of up to a few microns. Planar photonic crystals are usually fabricated in SOI featuring a silicon device layer of 200-400 nm thick, to ensure single mode operation. The presence of higher modes would collapse their bandgap. The buffer-oxide layer is usually at least 1um thick, in order to minimize radiation losses into the substrate. The requirement of a thin device layer and a thick buffer layer excludes many of the SOI wafers commonly produced for the microelectronic industry, where a large buffer thickness is not necessary. Silicon on insulator wafers manufactured by the BESOI (Bonded and Etched Back Silicon On Insulator) technique cannot be produced with a sufficiently thin silicon layer. Wafers produced by SIMOX (Separation by IMplantation of OXygen) are available with suitably thin silicon layers but because of the limitations of the oxygen implantation technique to generate the buried oxide layer, it is difficult to create an oxide layer thicker than a few hundred nanometers. The wafers used in this study have been fabricated by Soitec with their 'Smart Cut' process [29], which combines thermal oxidation to create a thick buried oxide with ion implantation to accurately define a thin silicon layer. These wafers have a 340nm silicon device layer and a 1um buried oxide.

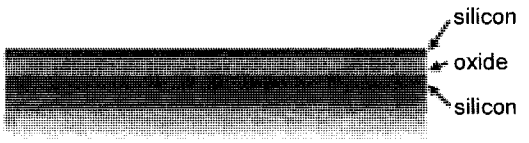

Figure 3.1: Cross-section of an SOI wafer. A single crystal silicon film is isolated from the bulk silicon substrate by an oxide layer.

3.3 Fabrication process flow summary

The fabrication of 2D photonic crystals is a conceptually simple process (Figure 3.2). Ten millimeter square diced SOI chips were first cleaned in Piranha solution (1:3 H_2O_2:H_2SO_4) to remove any residual organics. Microchem PMMA 950K A2, a common electron beam resist, was then spun onto the chip at 500 rpm for 5 s, at 4000 rpm for 30 s, and then

baked on a hotplate at 185°C for 5 min to remove any residual solvent. This yielded a resist layer thickness of approximately 90 nm. The PMMA was then exposed using a Raith 150 electron beam lithography system with an accelerating voltage of 2 kV, an aperture of 20 μm, and an electron dose of 24 $\mu C/cm^2$. Following exposure, the resist was then developed with a Microchem 1:3 MIBK:IPA solution for 30 s followed by a 15 s IPA rinse. The chip was then bonded with Fujifilm HPR 504 to a carrier wafer for insertion into the RIE systems. The carrier wafer was masked with HPR 504 to ensure that the amount of exposed silicon in the reaction chamber remained relatively constant. Areas of the SOI wafer exposed in development were then anisotropically dry-etched in an ICP-RIE. After the completion of the silicon etch, the remaining PMMA was stripped with acetone in an ultrasonic bath.

Butt-coupling from the fiber to the strip waveguide requires the exposure of the waveguide cross-section. Dicing the chips with a dicing saw results in unacceptable roughness of the edge facets, so the waveguides were instead cleaved along the crystal planes by hand. Prior to characterization, the photonic crystal slab was again cleaned in Piranha solution to remove surface contaminants.

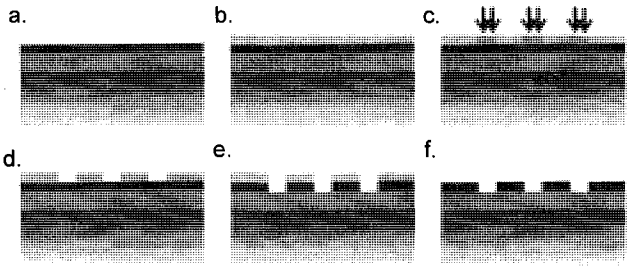

Figure 3.2: Silicon PPC fabrication: (a) beginning with clean SOI wafer (b) spin on PMMA (c) expose PMMA (d) develop PMMA (e) etch silicon (f) strip resist.

Optionally, one can partially release the silicon layer from the substrate with an HF oxide etch. This step was omitted to preserve mechanical robustness (particularly with regard to the waveguide tapers). A light thermal oxidization of the silicon after fabrication has been reported to reduce the loss of the waveguides [30]. This step was, however, also omitted to simplify the fabrication procedure.

3.4 Electron Beam Lithography

High resolution patterning is necessary to create photonic crystals with feature sizes smaller than 100 nm. While deep-UV exposure of photonic crystal waveguides has been demonstrated [31], the technique is not well suited for the research environment. Exposure by electron beam lithography (EBL) is usually employed.

Electron beam lithography is a direct-write process whereby an electron beam (having an accelerating voltage ranging from 1-100 kV) is scanned across a resist, altering the local chemistry. The achievable resolution is limited by the resist characteristics and the electron dynamics, rather than by the diameter of the beam itself. The most common approach for the fabrication of fine features relies on using a thin resist layer and a high beam energy in order to minimize forward beam scattering.

3.4.1 Low energy exposure dose

As electrons penetrate the resist and the substrate below, they scatter as they interact with the surrounding atoms. An electron may undergo forward scattering, where the electron is inelastically deflected by a small angle, generating secondary electrons. It may also be backscattered, elastically undergoing a large angle deflection. These effects are responsible for distributing the electron dose over an area larger than the incoming beam. Backscattered electrons contribute dose to neighboring areas of the resist, a phenomenon referred to as *proximity effect* [31]. Photonic crystal structures are very dense (even relative to modern CMOS devices) such that the proximity effect contributes significant dose to adjacent structures. The result is that interior holes of a photonic crystal tend to receive more dose than those at the edge, unevenly exposing and distorting the boundary holes (Figure 3.3).

The proximity effect is a nearly universal issue for patterning of photonic crystals. It can, however, be inhibited by proactively scaling the exposure dose, such that the net effect is an even dose distribution [32]. Low-energy exposure can also greatly reduce the proximity effect while maintaining high resolution [33]. This approach, using a low energy beam (2 kV accelerating voltage) to expose the PMMA layer, has been taken to counteract the proximity effect encountered in this work. Low energy electrons have significantly reduced

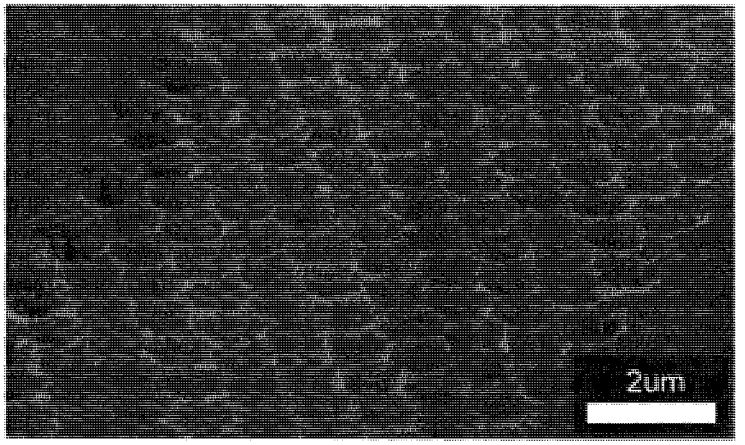

Figure 3.3: Silicon photonic crystal patterned at 10 kV without proximity effect correction. Holes at the boundary have not developed completely as they have received less dose than interior holes.

penetration depth (and reduced scattering) but at 2 keV are still sufficiently energetic to expose the full depth of the PMMA. Figure 3.4 presents a comparison of an equivalent number of electron trajectories for 2 kV and 10 kV electrons simulated using CASINO [34], a Monte Carlo based electron trajectory simulator.

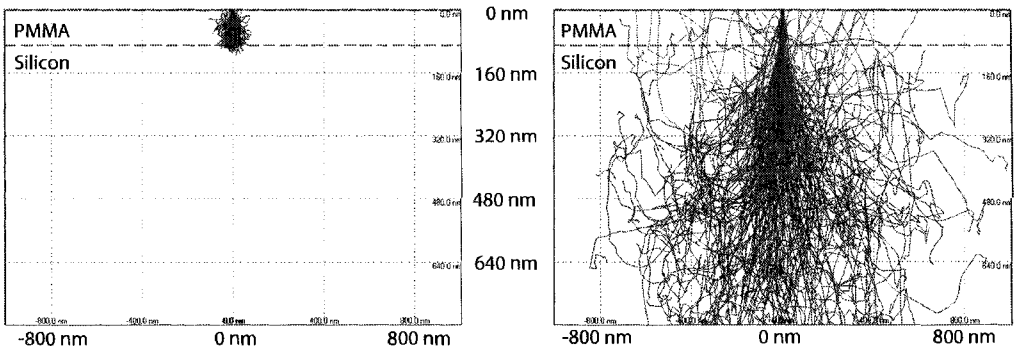

Figure 3.4: Computed electron paths for 200 electrons accelerated by 2 kV (left) and 10 kV (right). The 2 kV beam has a large high-dose area inside the resist but also exhibits less backscattering of electrons to adjacent areas of the resist. The horizontal dashed line represents the extent of the 90 nm PMMA resist layer.

Using low-energy electrons decreases the proximity effect at the expense of increased effective beam diameter. The resolution was, however, found to be more than sufficient for the high resolution patterning of photonic crystals devices (Figure 3.5).

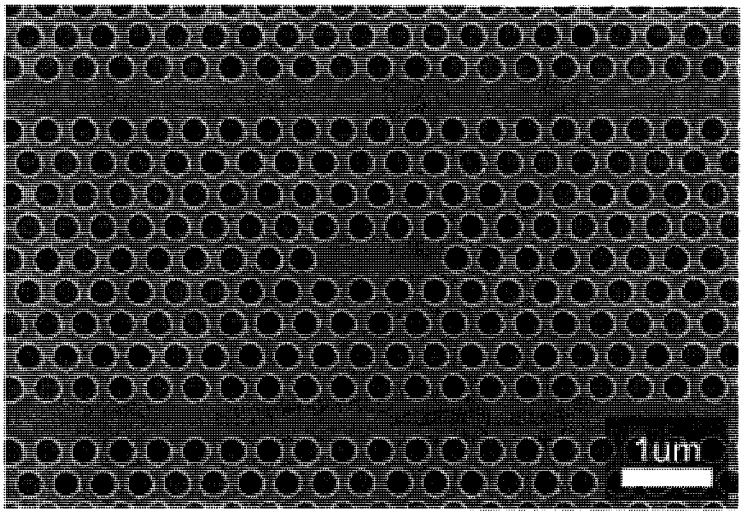

Figure 3.5: photonic crystal nanocavity patterned using a 2 kV exposure without proximity effect correction. Holes appear uniform in all areas of the exposure.

Due to the finite size of the electron beam, photonic crystal holes are defined in the design layout to be slightly smaller than the intended final product. The ultimate size of the holes can be finely tuned by judiciously overexposing each hole (Figure 3.6, 3.7).

Slight overexposure was found to smooth out non-circularities from the discretization of the electron beam movement (Figure 3.8). The extreme case, where only a single central point is exposed, was found to be less flexible as the tone of the resist reverses (resulting in image reversal) with sufficiently high dose, limiting the achievable diameter of the patterned holes to less than $\approx$300 nm.

3.4.2 FBMS waveguide exposure

Unlike photolithography, electron beam lithography is a serial process whereby every point is exposed sequentially within the beam deflection range, known as a write field. Large patterns are created by aligning (stitching) together multiple write fields. The error in aligning write fields is usually small, but even small errors will cause unacceptable phase jumps in the photonic crystal [7]. Critical regions must therefore be placed within a single write field, preferably near the center to minimize beam distortion. Large and complicated structures can take a significant time to expose, limiting the number of devices which can be created within a reasonable time.

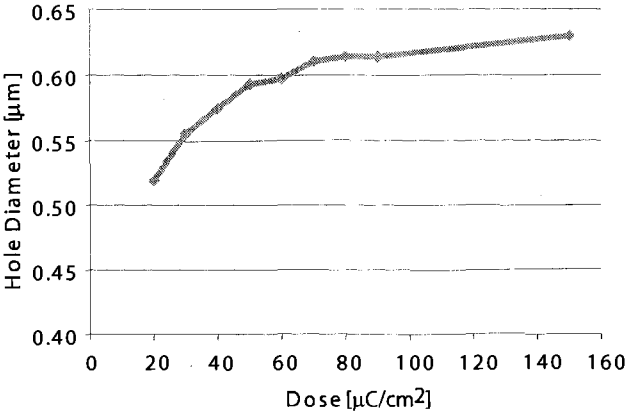

Figure 3.6: The relation between electron dose and resulting hole size. Holes patterned with nominal diameter 0.46 μm. The size of the hole grows, saturating at high dose.

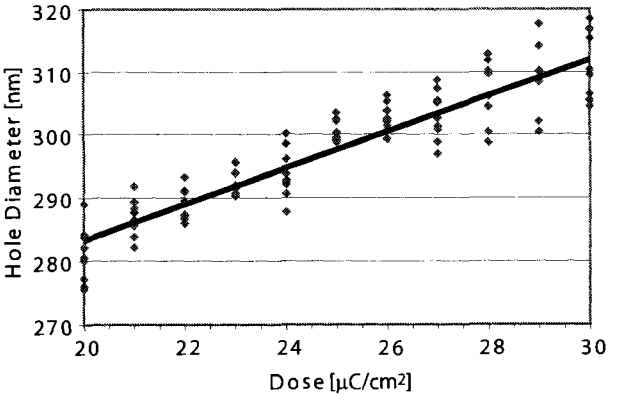

Figure 3.7: Fine scale relation between electron dose and resulting hole size. The hole diameter can be finely tuned with small changes in the dose.

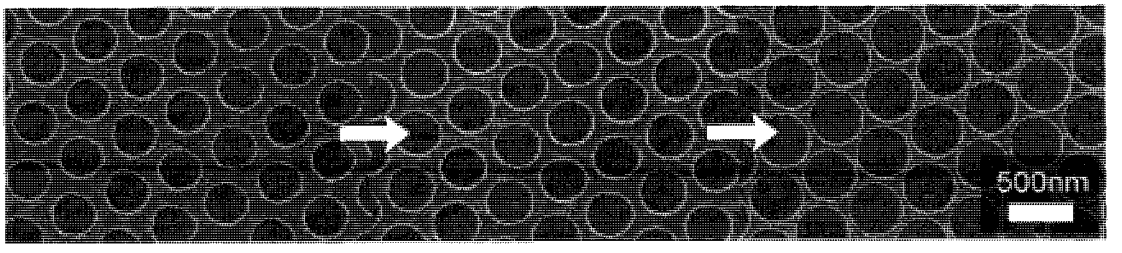

Figure 3.8: Silicon photonic crystals patterned with increasing dose from left to right representing the range from the minimum dose for full exposure to a saturated dose. As the dose increases the holes become larger and defects in their circularity are smoothed out.

The strip waveguides (defined by two 4 um lines) used to couple into the photonic crystal are comparatively simple structures. Patterning them with the same accuracy as the photonic crystal structure would consume a wasteful amount of writing time. As an alternative to scanning mode exposure, these waveguides have rather been patterned in fixed-beam moving stage (FBMS) mode, where the electron beam remains still or follows a fixed path while the stage moves below it. In this case, the two 4 um lines (Figure 3.9) have been exposed by an electron beam that continuously transcribes a 4 um diameter circle while the stage moves.

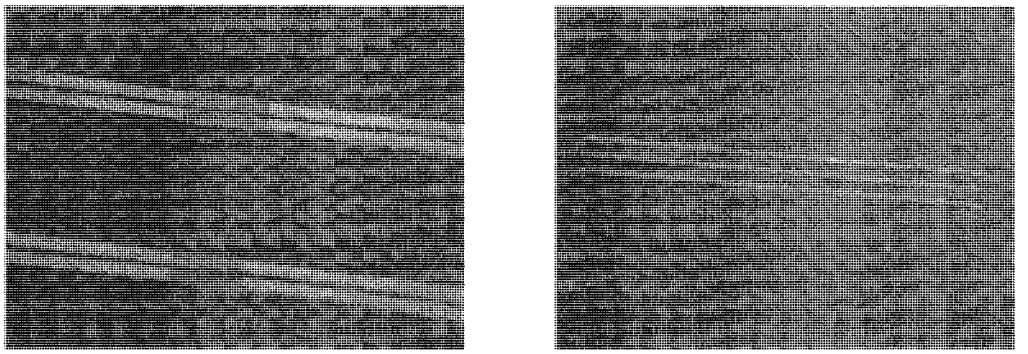

Figure 3.9: Photonic crystal waveguides coupled to tapered strip waveguide patterned in FBMS mode. The total length of this structure is 5 mm.

Fixed beam exposure of waveguides was found to be significantly quicker than scanning mode, and also eliminates the possibility of write field alignment errors appearing periodically along the waveguide. Quicker exposure makes the patterning of long waveguides feasible, simplifying the cleaving process required to expose the end facets and allowing more devices to be patterned within a fixed time period.

3.5 Nanoscale dry silicon etching

Once the photonic crystal pattern has been defined in the resist, it needs to be transferred to the underlying silicon layer with great accuracy. Inductively coupled plasma reactive ion etching (ICP-RIE) was chosen to etch the silicon. Dry etching is essentially a combination of chemical etching and sputtering. ICP-RIE allows the tuning of chemical and physical etch rates such that it is possible to gain precise control over the etch characteristics. The

inductive plasma coupling of an ICP-RIE allows the plasma density to be increased without affecting the energy of the bombarding ions.

A photonic crystal etch process needs to meet three basic criteria. Firstly, it should produce vertical sidewalls, such that the properties of the photonic crystal are constant throughout the slab. Secondly, it should produce sidewalls with low roughness. The silicon-air interface represents a very large refractive index discontinuity where even roughness on a scale much less than the wavelength of light becomes a significant source of scattering loss. Lastly, the etch process should have a good selectivity to the masking layer. Ideally the masking layer would be resist, though an intermediate masking layer may be required to etch deep structures, at the expense of increased fabrication complexity.

Silicon photonic crystal etching was demonstrated in this work using two methods, an SF_6/C_4F_8 reactive ion etch ('Unswitched' process) and a cryogenic SF_6/O_2 reactive ion etch ('Cryo' process), both of which yielded acceptable results. The SF_6/C_4F_8 process sacrificed resist mask selectivity but proved to be simpler and more reliable than the Cryo process. Except where specifically noted, the 'Unswitched' etch was used to create the photonic crystals reported here.

3.5.1 Cryo silicon etch

The cryogenic silicon etching process (Cryo etch) was first demonstrated by Tachi et al. in 1988 [35]. It uses an SF_6/O_2 plasma to etch silicon with fluorine radicals (forming volatile SiF_4) while inhibiting sidewall etching with the formation of a SiO_xF_y layer. This process relies on cooling the wafer below -100°C, reducing the chemical reactivity and enhancing the side-wall etching inhibition [36] such that passivation and etching can be balanced to vertically etch silicon. The Cryo process is highly selective to resist (>15:1) and to oxide (>30:1) [37] making it particularly suitable to applications requiring deep etching or thin resist masks.

Cryo etching was performed with an Oxford Plasmalab 100 ICP-RIE. Immediately prior to etching, an HF dip was performed to remove any native oxide which would unintentionally mask the silicon surface not removed. The reaction chamber was held at a fixed pressure of 7.5 mTorr while SF_6 and O_2 were injected a rate of 45 sccm and 10 sccm

respectively. The substrate was cooled with a helium backflow to a temperature of -110°C. The plasma was energized with a 400 W ICP power and a forward RF power of 6 W. The resulting etched structure appears of high quality with smooth sidewalls, though there is typically a small undercut of the resist by about 20 nm (Figure 3.10, 3.11).

3.5.2 Unswitched Bosch-like process

Deep silicon etching with the Bosch-process [38] is widely used in the fabrication of silicon MEMS. This process alternates etching silicon with fluorine radicals generated from SF_6 and depositing a fluoropolymer generated from the C_4F_8 plasma. Vertically oriented ion bombardment in exposed areas removes the passivating polymer allowing etching to occur at the bottom of exposed areas while leaving sidewall surfaces protected. The discrete etching and polymerizing steps of this process cause scalloping of the sidewalls, making them unsuitable for nanophotonic applications. The same process gases can, however, be used simultaneously in order to achieve continuous vertical etching.

A modified version of the Bosch dry etch where both steps occur simultaneously in a continuous process was performed with a Stanford Technical Systems ICP-RIE. Silicon was etched at room temperature under vacuum in a chamber held at a pressure of 20 mTorr, with gas flow of 80 sccm C_4F_8 and 110 sccm of SF_6. The plasma was energized with 2.5 kW of ICP power and 20 W of forward RF power. The selectivity of this process (approximately 1:8 for PMMA) is not as good as for the Cryo process but given the relatively shallow etches required, remains workable. Reduced etch selectivity also eliminates the necessity of a pre-etch HF dip, simplifying the fabrication process. The sidewall roughness of this etch process (figure 3.12, 3.13) is similar to that of the Cryo process. By eliminating the necessity of an HF dip and eliminating the time necessary to cool the reaction chamber, this process was much faster than the Cryo process. Being quicker and more reliable than the Cryo etch process, the 'Unswitched' process was chosen for all applications not requiring maximum resist selectivity.

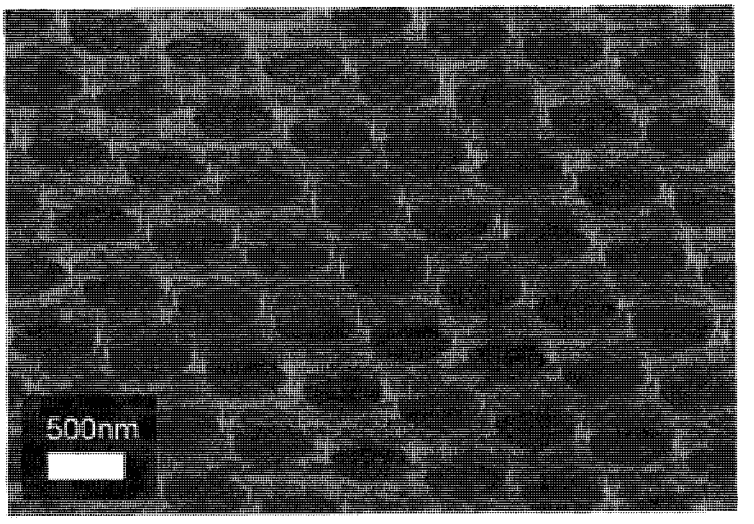

Figure 3.10: Photonic crystal patterned in SOI with the Cryo silicon etch process.

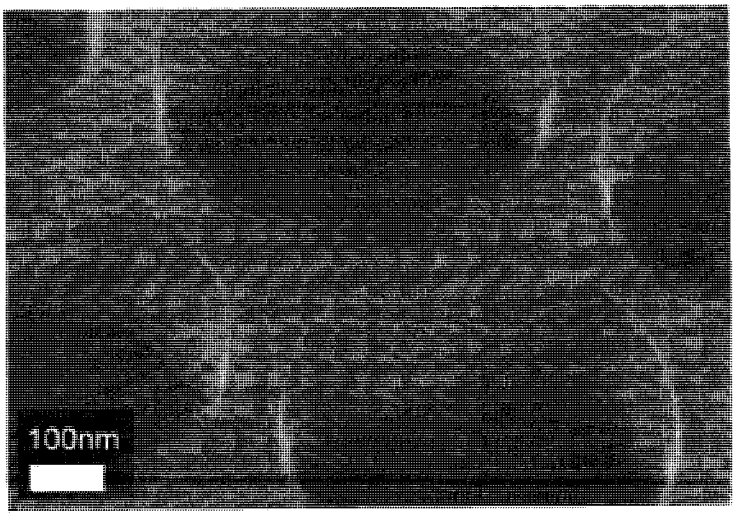

Figure 3.11: Close-up of photonic crystal patterned in SOI with the Cryo silicon etch process. Undercutting is visible at the top surface.

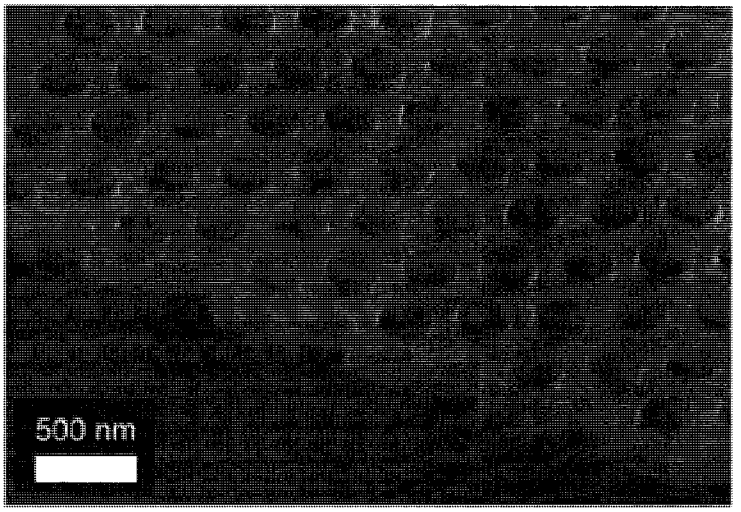

Figure 3.12: 'Unswitched' etch recipe result for a photonic crystal slab.

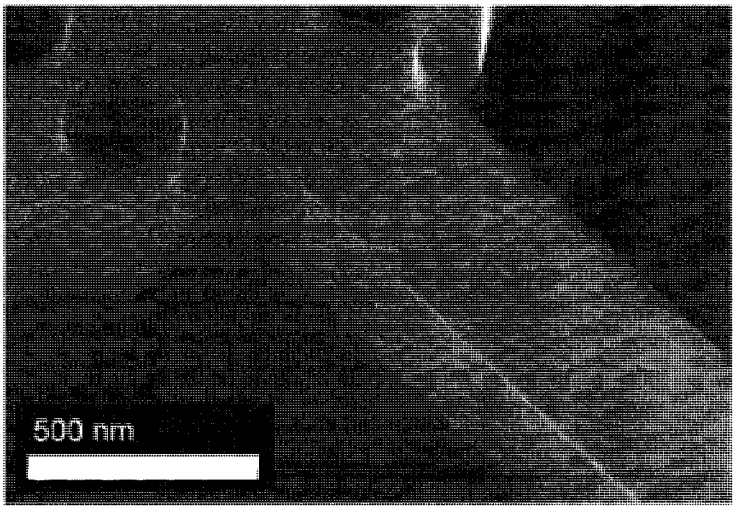

Figure 3.13: 'Unswitched' etch recipe result for a photonic wire interface showing the typical etch sidewall roughness.

3.6 Summary

This chapter outlines the fabrication procedure for creating silicon photonic crystals with a bandgap in the infrared regime. The two key process technologies involved in creating these structures are electron beam lithography and deep silicon etching. Rather than adaptively scaling the deposited electron dose, a low energy (2 keV) beam was used to pattern a PMMA film with greatly reduced proximity effect. FMBS mode exposure of waveguides was used in relatively low detail areas, significantly reducing exposure time. Nanoscale silicon etching was demonstrated using two distinct approaches, the 'Cryo process' and the 'Unswitched Bosch-like process'. Both approaches were shown to produce sufficiently high quality etches; however, the 'Unswitched' process was chosen for the bulk of the work presented here as it was found to be more reliable.

4

Observation of Photonic Bandgap Guidance

4.1 Introduction

Photonic crystal waveguides created by removing a row of air holes were fabricated using the procedure described in Chapter 3. These waveguides have been designed such that the cut-off of the lowest order photonic bandgap guided mode falls near λ_o=1570 nm, the midpoint of the tunable laser's range. This mode cut-off was observed to verify the successful creation of photonic crystal waveguides.

Because large scale patterning of photonic crystals remains challenging, silicon strip waveguides have been used to couple to relatively short photonic crystal waveguides (Figure 4.1). A large optical mode mismatch between the PCW and strip waveguide stands to create significant transmission losses. To improve the coupling, the strip waveguides taper from 2 μm wide at the cleaved interface, to 450 nm wide at the interface with the photonic crystal.

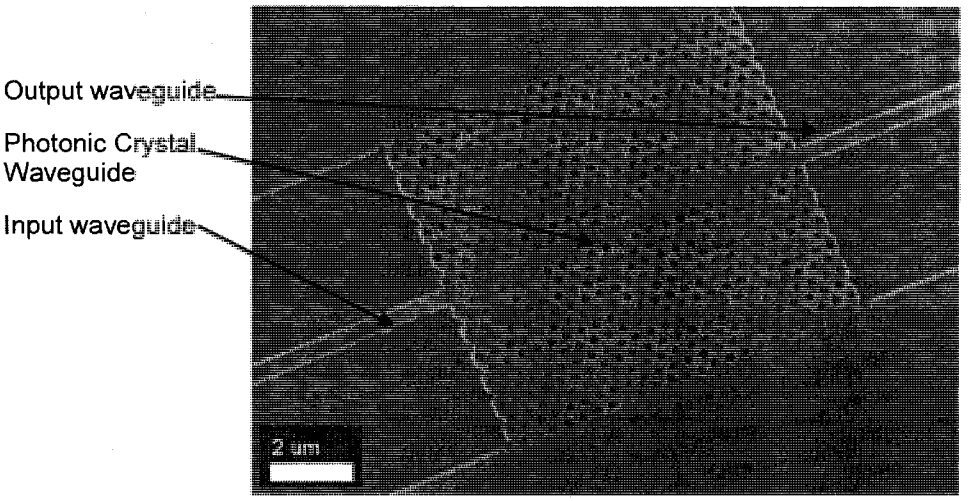

Figure 4.1: Silicon photonic crystal waveguide coupled to a tapered silicon strip waveguide.

4.2 Optical measurement setup

The spectral transmission response of the photonic crystal waveguides was tested using a custom coupling apparatus (Figure 4.2). A Santec TSL-210V tunable (1510-1630 nm) continuous-wave laser acts as the light source. The polarization state of the source was set with a Thorlabs looped-fiber polarization controller. The optical fiber used here is not polarization maintaining, so the polarization is set using a polarizing beam cube placed at the tapered fiber output, then removed prior to waveguide coupling.

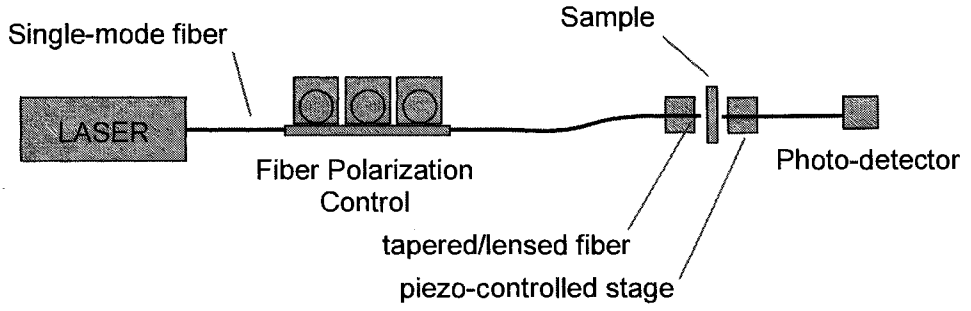

Figure 4.2: Waveguide alignment setup for coupling a tunable laser to an on-chip waveguide and collecting the transmitted output.

The silicon strip waveguide mode was excited by butt coupling. At 9 μm, the core diameter of a standard SMF-28 fiber is poorly matched to the silicon strip waveguide, which has a thickness of only 0.34 μm and a width of 2 μm. To increase the coupling efficiency, the beam was focussed upon the end facet with an Oz Optics antireflection coated tapered and lensed fiber (Figure 4.3). The fibers were then aligned with piezoelectrically controlled 3-axis translation stages and a 20X long working distance objective. Coarse alignment was achieved visually with the objective and a camera. Fine tuning was performed by maximizing transmitted power. In the same manner as light is coupled into the strip waveguide, output light was collected with a tapered/lensed fiber and transmitted to a Newport InGaAs photodetector. The spectral response was measured by recording the transmitted power as the laser output wavelength was scanned. Data collection and laser tuning was automated using a custom LabVIEW controller.

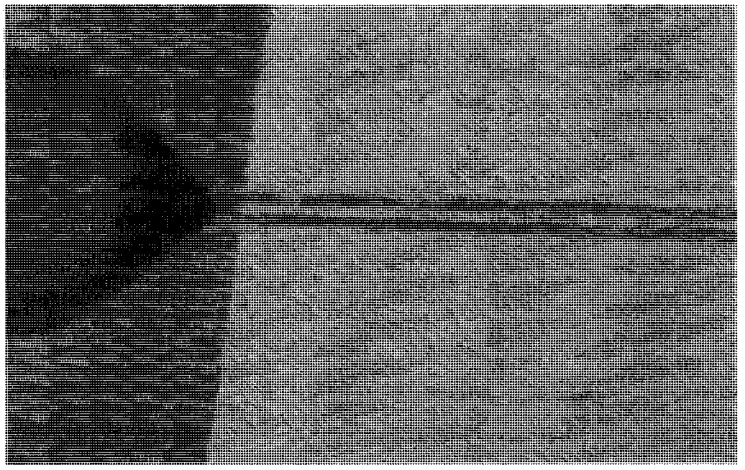

Figure 4.3: Tapered/lensed fiber aligned and focused for coupling to a 4 μm wide silicon strip waveguide.

4.3 Observation of the photonic crystal waveguide mode cut-off

Evidence of planar photonic crystal waveguides operating in the infrared regime was first reported by Baba et al. in 1999 [39]. An important objective of this work was to likewise experimentally observe waveguide guidance by the photonic bandgap effect.

A mode cut-off was successfully observed at 1553 nm for a W1 photonic crystal waveguide (Figure 4.4). This value is in agreement with the predicted position of 1530 nm as simulated by a 3D plane-wave expansion (Figure 4.5). Versus the simulation, the holes are slightly larger (r=0.38a) and the slab is slightly thicker (t=0.85a), accounting for the $< 2\%$ deviation. The observed transmission spectrum is of the same form as predicted by FDTD simulation in Figure 4.6. Fabry-Perot oscillations are visible throughout the spectrum due to the formation of a standing wave between the cleaved waveguide edge and the photonic crystal waveguide. These oscillations have been filtered from the results presented elsewhere in this report.

Photonic crystals are scale independent so by varying the lattice dimension, it is expected that the mode cut-off will shift correspondingly. This effect is demonstrated in Figure 4.7, where the transmission spectrum is plotted for waveguides with a crystal lattice of 394 nm and 400 nm. Ideally, the ratio of the lattice dimension to mode cut-off wavelength would be independent of the lattice size. In this case, the slab thickness does not scale with the lattice so the lattice/cut-off wavelength ratio is not constant.

Photonic crystals are polarization dependent and for the dimensions reported here, the bandgap only exists for the TE polarization. The transmission characterisitics of TM polarized light in this frequency range depend on the thickness of the silicon slab. For a thickness of 340 nm, a TM index contrast guided mode is expected. This guided mode was observed in the wavelength range of interest (Figure 4.8). As expected, index-guided TM polarized light does not experience a mode cut-off.

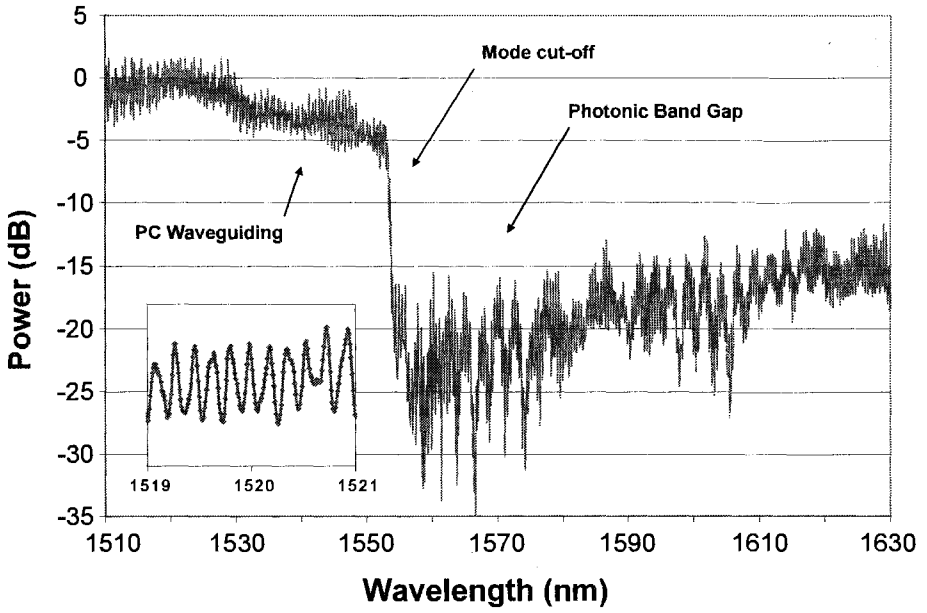

Figure 4.4: Transmission spectrum for a photonic crystal waveguide with period a=400 nm near the mode cut off. The transmission abruptly drops at the transition from the waveguide mode to the band gap. Inset is a close-up of the Fabry-Perot resonance present throughout the spectrum.

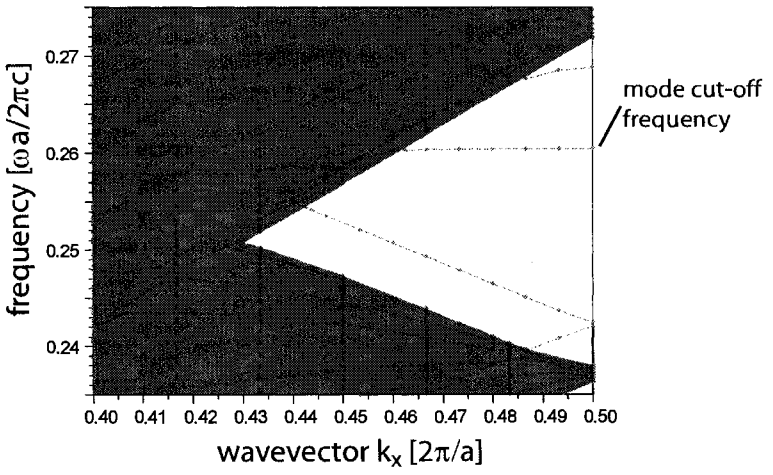

Figure 4.5: Projected band diagram for a silicon photonic crystal with hole radius 0.35a, slab thickness of 0.73a, clad asymmetrically with air and oxide. The shaded regions correspond to a continuum of states. The even mode photonic crystal waveguide mode is indicated.

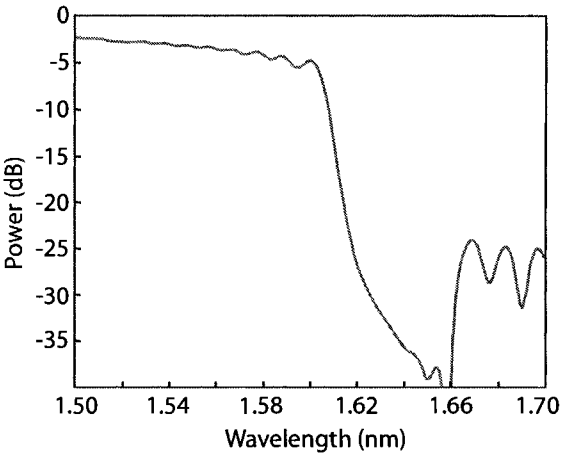

Figure 4.6: Transmission of a W1 photonic crystal waveguide with r=0.35a simulated with FDTD

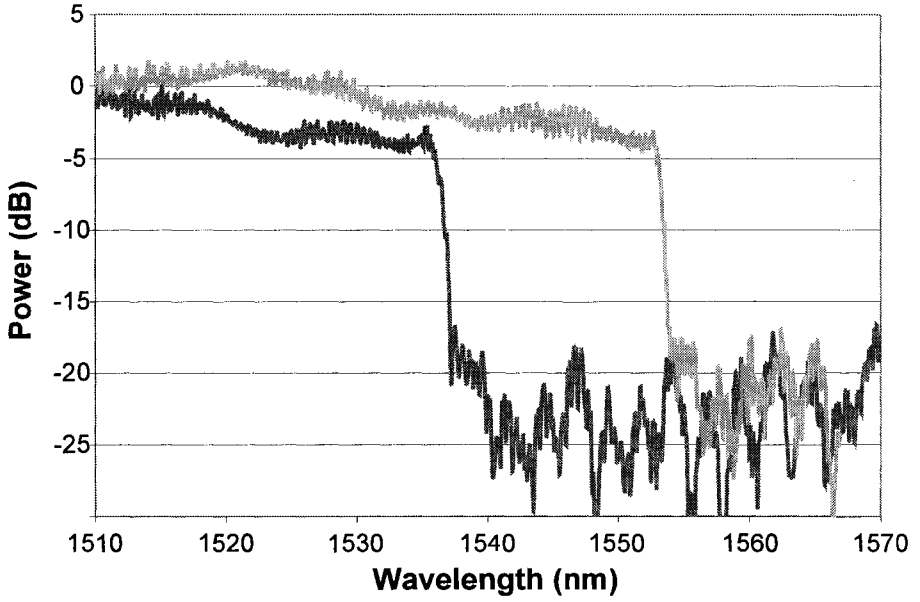

Figure 4.7: Photonic crystal waveguide mode cut-off for lattice dimensions of 394 nm (left) and 400 nm (right) The mode cut-off red-shifts as the lattice of the photonic crystal increases.

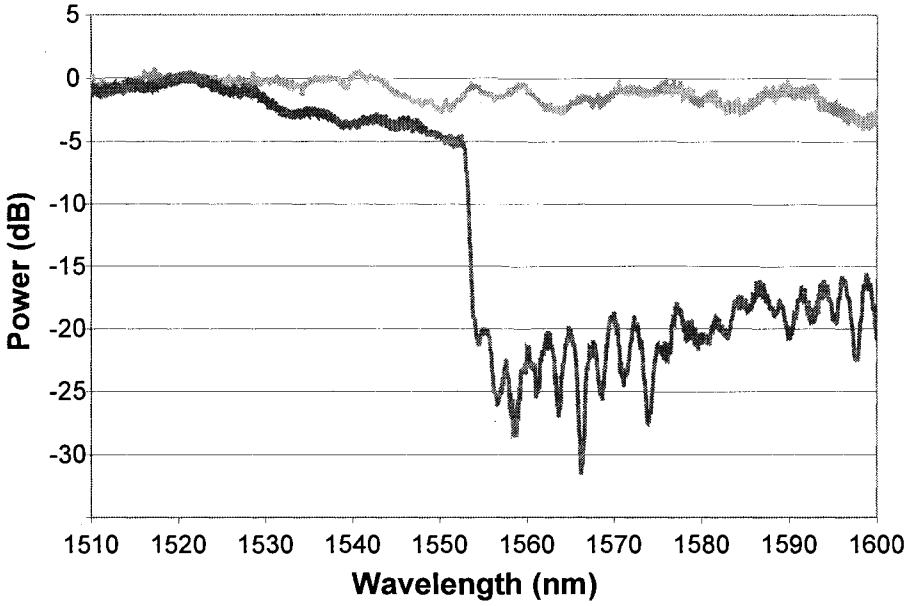

Figure 4.8: comparison of TE and TM propagation near the TE photonic crystal guided mode cut-off. TM polarized light is transmitted throughout the spectrum, inside the frequency range of the TE bandgap.

4.4 Summary

Photonic crystal waveguides were coupled to a tunable light source using lensed fibers and tapered silicon wire waveguides. A photonic crystal waveguide mode cut-off was experimentally observed in good agreement with theoretical predictions. This mode cut-off was observed only for the TE polarization as expected, and can be shifted in frequency by tuning the lattice dimension as expected.

5

Photonic Crystal Waveguide Biosensors

5.1 Introduction to biosensing

Optical sensing has broad application to many industrial and research settings. Since biological sensors were first reported in the early 1960s [40] there has been considerable growth in the field. The principal applications of biosensors include biological monitoring, biomedical diagnostics, and environmental sensing. Recent research has focused on creating sensors which can make sensitive, real-time, label free measurements of biological species. A successful biosensor should be capable of sensitive and specific detection with potential for multiplexing and manufacturable at low cost.

Two main markets primarily drive such development [41]. In the first, biosensors are of interest for the rapid detection of emerging pathogenic threats such as viruses [42], as well as water-borne [43], food-borne [44], and air-borne pathogens [45]. The second market has evolved from developments in genomics and proteomics which have enabled a proliferation of biomarkers identified with specific diseases [46–48] and pharmacological responses [49]. Though the absolute number of known biomarkers remains relatively small, the potential for multiplexed detection remains promising for screening against a large number of pathogens and for creating biomarker 'fingerprints'.

Biosensors have two fundamental components, a biological receptor and a transducer (Figure 5.1). The bioreceptor uses a biochemical recognition mechanism to selectively identify the target analyte and is generally classified to be in one of five categories: antibody/antigen, enzymes, nucleic acids/DNA, cellular structures, and biomimetic [50]. The transducer transforms the bioreceptor interaction into a measurable quantity. Most transduction approaches can be categorized in one of three classes: mass based detection methods, electrochemical methods, and optical methods.

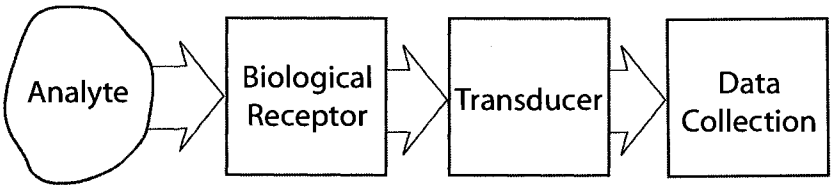

Figure 5.1: Principal components of a biosensing system. A bio-analyte is detected by a bioreceptor element. The transducer then transforms this interaction into a measurable quantity and the result is recorded.

A good biosensing system is both highly sensitive and highly selective. Linear biosensors are typically evaluated in terms of their resonant wavelength shift per unit refractive index shift (RIU) and their limit of detection (LOD) which may be quoted either as a mass or a mass concentration. Reducing the LOD of a sensor simplifies biological measurements as it can eliminate the need for target amplification [41].

5.1.1 Mechanical transduction

Mass sensitive transduction techniques typically operate by sensing a resonance frequency shift of a mechanical oscillator. Acoustic devices form one class of mechanical biosensor. Most of these devices exploit bulk acoustic waves (BAW), such as the quartz crystal microbalance (QCM) [51]. The QCM biosensor uses a piezoelectric quartz plate which has a vibrational resonance in the presence of an external electric field. Mass loading on the surface of the quartz plate causes the vibrational resonance to shift to a lower frequency. QCM detection limits are on the scale of ng/cm^2, with balance surface radii of tens of microns [52]. Surface acoustic wave (SAW) devices operate in a similar manner using shear surface waves and possess similar sensitivities [53].

Cantilever-based devices form another class of mass-detection biosensors. The high quality factors of resonant micro and nanomechanical systems are well suited to sensitive mass detection. In dynamic-mode, mass bound to a cantilever is sensed by a change in the resonant frequency of oscillation. To avoid problems related to viscous damping under air or liquid, static-mode deflection systems have also been developed [41]. These measurements rely on binding events along one side of the cantilever to cause the cantilever to induce static binding. Nanomechanical resonators have been employed to detect DNA strands [54], single cells [55], and viruses [56]. Yang et al. specifically demonstrated the ability of nanomechanical cantilevers to measure mass with a detectable limit of 20 zg, with a resolution of 7 zg [57].

5.1.2 Optical transduction

Optical biosensing transducers can be devised to employ virtually any optical property [50], though the primary approaches rely on spectroscopy of absorption [58], fluorescence [59], phosphorescence [60], refraction [61], Raman [62], and surface enhanced Raman scattering [63]. Current optical biological detection techniques are usually based on the use of radioactive or fluorescent labels. Using these labels is often labor intensive and slow, so a recent trend in biological sensing research has been to move toward 'label-free' techniques, which stand to reduce complexity and decrease the potential of contamination [64].

Refractive index sensors detect the presence of an analyte by a shift in the local refractive index. Guided wave sensors can be highly sensitive to changes in the index at the waveguiding surface. This is desirable for sensing very thin layers as is usually the case for surface immobilization biosensors [65]. The response of a guided wave sensor falls off logarithmically away from the surface.

Because the market for integrated biosensors is relatively small, it is not generally economical to develop a distinct sensing system for every application. The preferred approach is to instead develop sensing platforms which can be used in a variety of applications [66]. The most prevalent tool for localized refractive index sensing is the

surface plasmon resonance (SPR) sensor [67] where an index shift near a metal surface alters the efficiency of surface plasmon coupling which in turn changes the reflectivity of the surface.

5.2 Photonic crystal biosensors

Photonic crystal devices have recently received increasing attention for biosensing. Photonic crystal fibers (PCF) have been demonstrated for sensing antibodies [68] and DNA [69]. These fiber sensors are, however, difficult to implement in a compact, automated manner. Bulk photonic crystal structures have also been reported for similar applications. In this case, white light reflectometry is used to detect bandgap shifts due to the immobilization of proteins [70] and antibodies [71].

More recently, planar photonic crystals have also been presented for biosensing applications. Here, the addition of a thin surface film affects the local refractive index, changing the effective refractive index of the slab and the refractive index contrast between the 'hole' and 'slab' regions. As most of the field power is centered in the slab, the response is dominated by this sidewall deposition [72].

Planar PC biosensors can tightly confine light, increasing analyte interaction and decreasing the interaction volume of the sensor. Limited interaction volume is favorable when working with small analyte volumes and stands to increase the achievable temporal resolution of real-time detection schemes. Additionally, planar two-dimensional silicon photonic crystals can be fabricated using existing microelectronic fabrication processes, ensuring that they are well suited for integration with microelectronic or other photonic devices [72] and with an integrated with a microfluidic delivery system [73].

5.2.1 Planar photonic crystal resonant cavity sensors

Photonic crystal cavities have already shown considerable promise for biosensing within extremely small volumes. They can confine light to a small modal volume for a long time such that there is a very strong material interaction with the trapped photons. Tight confinement and strong interaction increase the sensitivity of the device such that very small refractive index shifts can be detected.

Planar 2D photonic crystal microcavity sensors have been demonstrated as biological thin film sensors [73,74] and as single particle sensors [72]. Reports thus far have employed variations upon photonic crystal cavity structure demonstrated by Chow et al. in 2003 [75] (Figure 5.2). The photonic crystal cavity is created by shrinking a single hole in a hexagonal lattice photonic crystal slab. This cavity is coupled by strip waveguides aligned in the ΓM direction. Correspondingly, the optical transmission spectrum has a narrow transmission peak inside the bandgap. The center frequency of the resonance will be affected by the refractive index inside the pores. The photonic crystal defect cavity strongly localizes light such that the sensor is most sensitive to a thin film near the defect and its immediately adjacent holes [64].

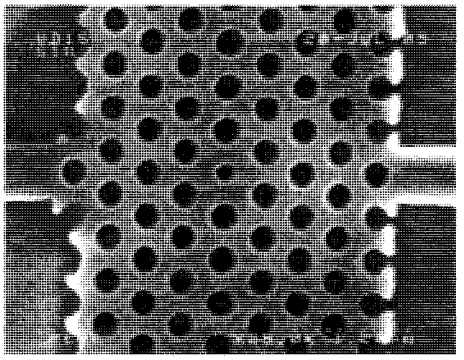

Figure 5.2: Photonic crystal nanocavity sensor formed by a single point defect reported by Mirkarimi et al. [73]. All nanocavity biosensors reported thus far have been variations on this design. Copyright [2006] IEEE. Reprinted from the Digest of the 2006 LEOS Summer Tropical Meetings, Toward single molecule detection with photonic crystal microcavity biosensors, L. Mirkarimi et al.

Biological sensing with planar photonic crystals has been demonstrated using biotinilated bovine serum albumin (BSA)/antibiotin [73], glutaraldehyde/BSA [64], and biotin/streptavidin [64]. Lee et al. recently demonstrated the attachment of a 1.5 nm layer of BSA to a 0.7 nm layer glutaraldehyde, with a corresponding resonance red shift of 1.7 nm and 1.1 nm respectively. Assuming a monolayer thickness deposited over a surface area of 50 μm^2, the sensed protein mass was determined to be 2.5 fg, significantly more than the detection limit of SPR, but using a much smaller sensing area [64].

Real time biological binding measurements have been reported with an integrated microfluidic flow cell. Mirkarimi et al. have reported the real time binding of antibiotin

to an immobilized biotinylated BSA delivered by a prototype microfluidic channel [73]. They measured a 1.1 nm resonance shift for a partial monolayer deposition and were able to detect the binding of 24 molecules with a 0.05nm shift. The modal volume of the sensor was a mere 33 attoliters.

Photonic crystal cavity devices are sensitive enough to measure single particles. Lee et al. recently demonstrated a photonic crystal cavity with a (still relatively low) Q of 2000, enabling the detection of particles with a diameter ranging from 50 to 500 nm, and measuring masses as small as 0.05 fg with a sensing area of only 40 μm^2 [72, 76]. A single 370 nm latex sphere, roughly approximating the dimensions of a virus particle, was detected as a proof of concept [76]. The size and attachment position of the particle both affect the cavity resonance shift creating an ambiguity in the interpretation. As with many other single particle detection schemes, practical application will require additional refinement to particle localization.

With extremely high Q cavities comes the potential for extreme sensitivity to small refractive index shifts. The extreme sensitivity of PPC cavity sensors also presents a liability. Irregularities in manufacturing will shift the resonance peak just as the target species may. Fabricating cavities with the precise intended resonance frequency remains a significant challenge [65]. Post-fabrication tuning would almost certainly be required to produce a consistent product.

5.2.2 Planar photonic crystal waveguide sensors

Photonic crystal waveguides have been demonstrated for nanofluidic tuning [77], refractive index measurements [78], and detection of liquid crystal orientation [79]. Recently the PCW has also been demonstrated for biosensors. The dispersion characteristics of the typical single line defect photonic crystal slab waveguide are such that it is effectively single-moded, with a mode cut-off falling inside the photonic band-gap. In the transmission spectrum, this mode cut-off corresponds to an abrupt drop in the waveguide transmission. Any shift of the local refractive index at the surface of the photonic crystal waveguide will cause a corresponding shift of the mode cut-off wavelength.

A planar photonic crystal waveguide biosensor has been reported by Skivesen et al. in 2007 [65] where they demonstrated a waveguide mode cut-off shifting in response to a thin protein layer. Their W1 photonic crystal waveguide biosensor was found to have a bulk sensitivity of $\lambda_{co}/ n_c = 64$ nm/RIU to a homogenous cover layer.

To demonstrate the sensor's detection of thin protein layers, Skivensen et al. deposited a layer of bovine serum albumen (BSA) by nonspecific physical adsorption. The BSA layer was successfully detected as 0.2 nm and 0.4 nm mode cut-off red-shifts for 2.6 nm and 3.2 nm protein layer thicknesses, respectively.

The sensor demonstrated a surface coverage sensitivity of 6 ng/mm^2 which remains inferior to what is currently achievable with SPR (1 pg/mm^2) [80] and waveguide sensors (5 pg/mm^2) [81]. The authors noted, however, that the signal-to-noise is far above the detection limit and that there appears to be considerable room for improvement to the design.

A notable advantage of the photonic crystal waveguide sensor is that the fabrication requirements are somewhat relaxed versus the PC cavity biosensor, yet PCW sensors can still be made to be very compact and are integrable with other optical or electronic systems on a single chip [65].

5.3 Demonstration of PPC waveguide biosensing

To date there has only been a single demonstration of PPC waveguide biosensing. The results presented here build upon this work with the demonstration of *specific* biosensing as well as the demonstration of an improved architecture for increased sensitivity of the photonic crystal waveguide sensor.

5.3.1 Bulk sensitivity of photonic crystal waveguide sensors

Photonic crystal waveguide sensors are most sensitive to a change in the refractive index near the surface of the silicon. The response tapers off as the distance from the surface increases. The response of the sensor to an effectively infinite analyte layer therefore sets an upper limit to the sensitivity.

Figure 5.3 compares the simulated TE transmission spectra of a W1 silicon photonic crystal waveguide computed with the 2D FDTD effective-index method. Spectra are shown for a photonic crystal with air filled holes, compared to a photonic crystal with water filled holes. The wavelength of the mode cut-off red-shifts by 30 nm as the hole refractive index increases from n=1 to n=1.33.

To test the response to a change in the cover layer refractive index, de-ionized water (n=1.33) layer was dispensed onto the surface of the waveguide. The response of a photonic crystal waveguide is seen in Figure 5.4.

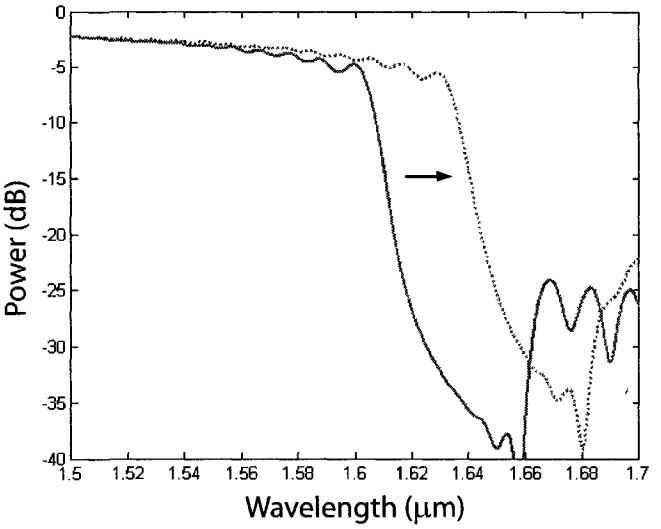

Figure 5.3: Transmitted power through a 24a long W1 photonic crystal waveguide for water (dashed) and air infiltrated (solid) holes as simulated by FDTD. A 30 nm red-shift of the mode cut-off is observed when the holes are filled with water.

The group index of the waveguide mode increases with increasing wavelength, diverging at the mode cut-off. Loss due to increasing group index makes distinguishing the high-loss region from the cut-off region increasingly difficult for the water-clad structure. As the mode cut-off has become less distinct with the addition of a water cover layer, point A is chosen as a reference. This point is believed to correspond with the onset of coupling to TM-like photonic crystal slab-modes [82, 83]. The measured shift due to a change in

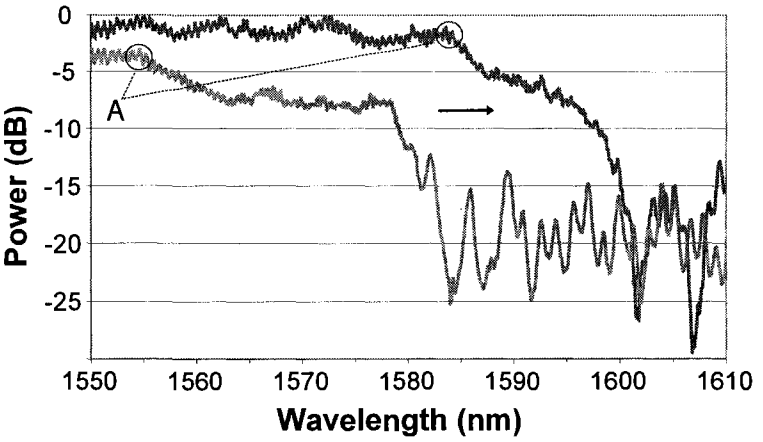

Figure 5.4: Photonic crystal waveguide mode cut-off given air-cladding (orange) and water-cladding (blue) Increased loss makes the mode cut-off less distinct, so point A was chosen as a fixed reference. The mode cut-off red-shifts under the water layer by 29nm.

the cover layer refractive index from 1 to 1.33 was 29 nm, yielding a bulk response of 88 nm/RIU. The responsivity reported here agrees well with the predicted response and with values reported by Skivesen et al. [65].

5.3.2 Silane thin-film detection

Donor-defect photonic crystal waveguides confine the majority of the field power within the silicon slab, with an evanescent tail penetrating into the surrounding material. As a result, the sensitivity rapidly declines away from the silicon surface. As a measure of the sensitivity in this close proximity region, a thin layer of 3-mercaptopropyltrimethoxysilane (MPTMS) was deposited to test the response. MPTMS forms a monolayer which was measured by ellipsometry to be 5.6 nm thick, assuming a refractive index of 1.44 [84]. The addition of the MPTMS layer red-shifts the photonic crystal waveguide mode cut-off by 3.2 nm (Figure 5.5).

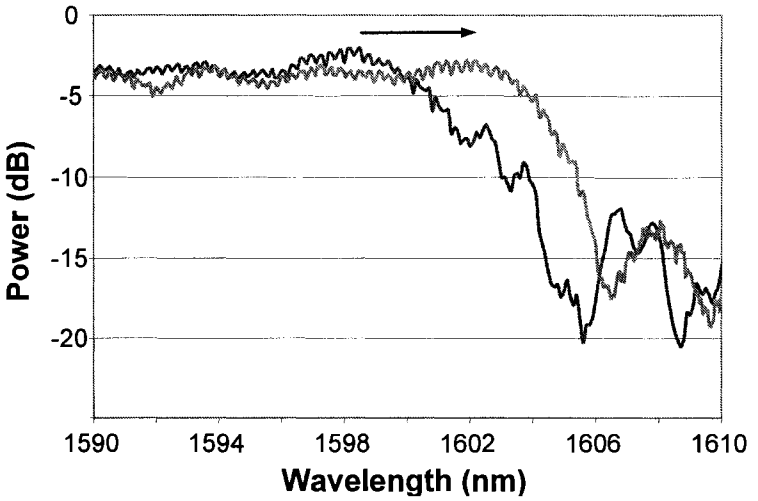

Figure 5.5: Detection of MPTMS layer. The mode cut-off for a bare silicon surface (blue) and with the addition of a 5.6 nm layer of MPTMS (orange). The mode cut-off red-shifts by 3.2 nm.

5.4 Biofunctionalization of PPC waveguide sensors

Biofunctionalization merges the photonic crystal waveguide transducer with a biological receptor. The biotin-streptavidin system is well documented and has been used here as a proof of concept. This system possesses a very high binding affinity and high specificity, with each streptavidin molecule having four biotin binding sites.

Beginning with a freshly piranha-cleaned Si substrate, MPTMS was deposited on a clean silicon surface, followed by the deposition of biotin, and then deposition of the target molecule, streptavidin. The biofunctionalization procedure employed here was developed and conducted by Dr. Vincent Wright of the Jillian Buriak group. Deposition begins by immersing the sample in a 20:1 toluene to MPTMS solution at 100°C, under Ar atmosphere, then rinsing with toluene, ethanol, acetone and drying with nitrogen. Second, the silanized samples were immersed for 1 hour in a 1 mg/mL concentration of biotin in a 1:1 dimethyl sulfoxide (DMSO)/phosphate buffered saline (PBS) and then rinsed with DMSO/water, ethanol, acetone and dried with nitrogen. Lastly, a 10 mM solution of

streptavidin in a phosphate buffer solution with 1% Triton X surfactant was diluted to 10 μM. With this solution, the biotinylated samples were exposed to the streptavidin solution for 1 hour, then rinsed with a PBS/Triton X solution, ethanol, and acetone and dried with nitrogen.

A second experiment was conducted to verify that the red-shift is due to specific binding of the streptavidin, rather than to the non-specific surface adsorption. Streptavidin has four binding sites to which the biotin can attach. A negative control experiment was conducted where pre-saturated streptavidin was flowed over the sensor. Binding between the surface biotin layer and the saturated streptavidin was not expected since all the binding sites of the streptavidin were already occupied.

The spectral transmission profile near the mode cut-off was recorded following biotin deposition and streptavidin immobilization (Figure 5.6). As expected, the mode cut-off red-shifts with the binding of the streptavidin layer. The streptavidin protein layer was successfully observed as a red-shift of 0.86 nm.

The negative control experiment confirmed that this shift was due to the specific binding of streptavidin, rather non-specific binding of streptavidin or another species. The result of this experiment is seen in Figure 5.7. Indeed, a very slight 0.1 nm blue-shift of the mode cut-off was observed, possibly as a result of a thin residue being removed in the process.

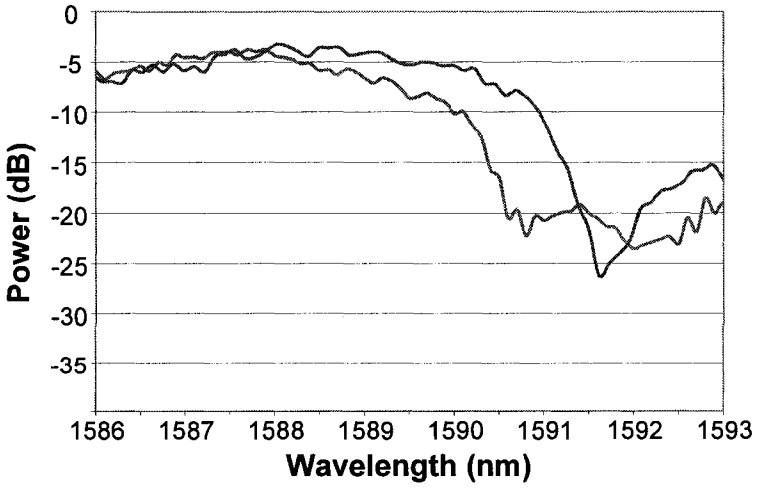

Figure 5.6: Photonic crystal waveguide mode cut-off following biotin deposition (red) and following streptavidin deposition (blue). The mode cut-off red-shift by 0.86 nm.

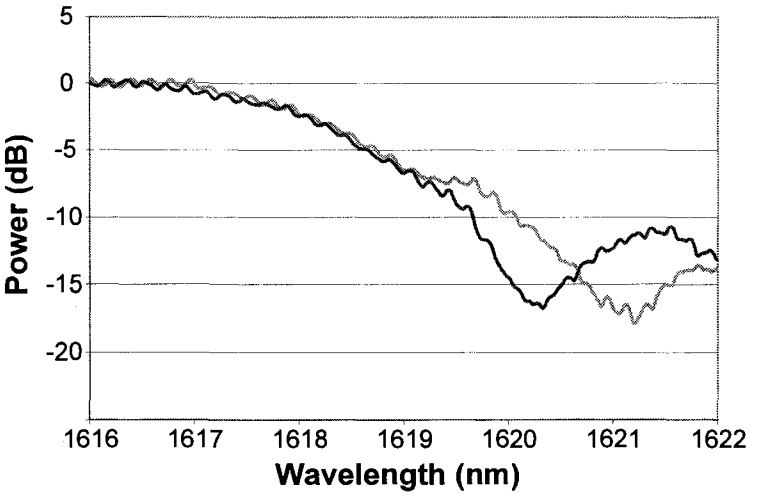

Figure 5.7: Mode cut-off for a photonic crystal waveguide after deposition of biotin (orange) and after the attempted deposition of a solution of saturated streptavidin (blue). The mode cut-off has not shifted significantly. The deviation between the two traces at low power is due to standing waves formed by TM polarized light.

5.4.1 Modified photonic crystal waveguide design for enhanced sensitivity

In order to improve the photonic crystal waveguide sensor's sensitivity, a modified donor-defect waveguide is presented, seen in Figure 5.8. Rather than eliminate a row of holes to form a photonic crystal waveguide, a set of holes are shrunk to a fraction of their original size. The behavior of this waveguide is similar to that of the W1 waveguide, except that the modes are shifted to higher frequencies inside the bandgap. This structure significantly increases the amount of surface area available for sensing in the 'high-field' regions, increasing its response to a shift in the ambient refractive index.

As before, the modified photonic crystal waveguide architecture was immersed in water to determine the bulk response to an effectively infinite homogenous film. This structure was fabricated with a lattice of 446 nm and hole radii 0.37a and 0.22a. A 41 nm shift was observed corresponding to a sensitivity of 120 nm/RIU, a 40% improvement relative to the W1 sensor.

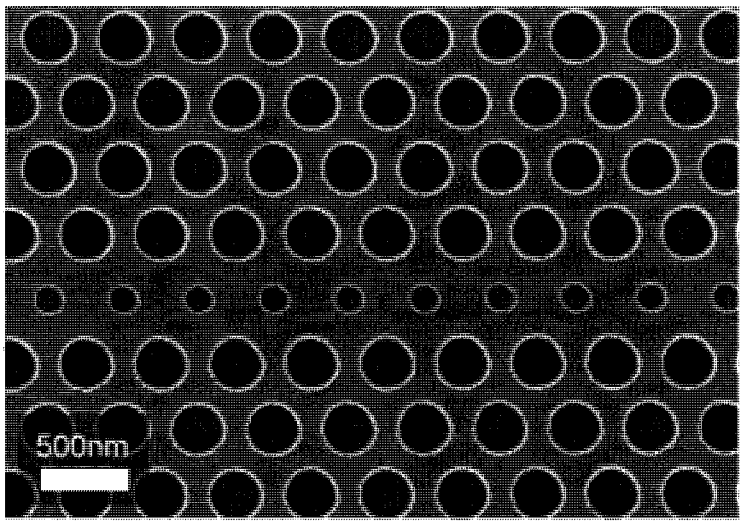

Figure 5.8: Photonic crystal waveguide sensor architecture for enhanced sensitivity. The lattice is 446 nm, with hole radii 0.37a and 0.22a.

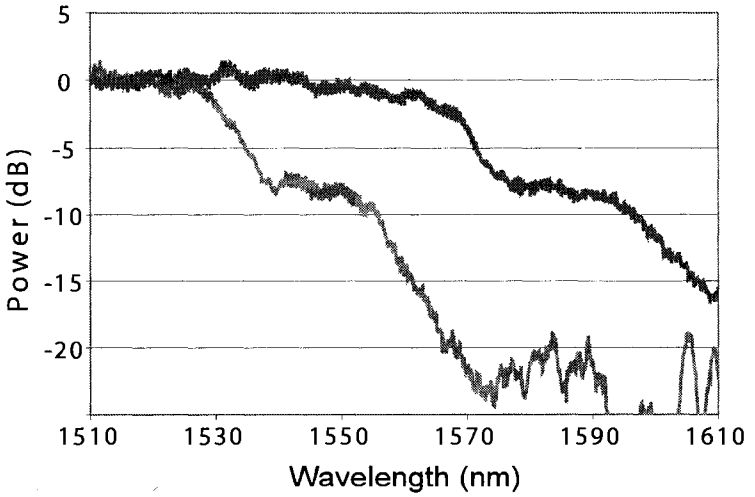

Figure 5.9: Modified photonic crystal waveguide response. The orange curve corresponds to transmission in air and the blue corresponds to transmission under water. The spectra red-shifts by 41 nm.

5.5 Future directions

The photonic crystal waveguides reported here were much longer than required to resolve the mode cut-off. In fact, the depth of the mode-cut off was limited by the polarization isolation rather than the waveguide length. Shortening the device would reduce the effect of increasing loss near the mode cut-off, making it easier to detect. Shrinking the photonic crystal waveguide sensor would also further reduce the sensing volume.

While such a structure does not appear to have been thus far proposed in the literature, it should also be possible to exploit the 'slow-light' dispersion of the photonic crystal to significantly increase the sensitivity of these waveguides. Interferometry using a Mach-Zehnder architecture (MZI) is a relatively common sensing approach to making highly sensitive phase-based measurements [85]. By placing the photonic crystal waveguide in the sensing arm, the output signal becomes dependent on the cumulative phase difference between the arms. Near the cut-off, the group velocity of the travelling mode decreases dramatically, falling to zero at the mode cut-off. This wave compression can be exploited to create compact MZIs, where the required interaction length is reduced by a factor of c/v_g [27]. Integrated silicon photonic crystal interferometers have been demonstrated with a group index of 80 [86]. Gigahertz bandwidth MZIs incorporating photonic crystal waveguides have been reported to reduce the interaction length by two orders of magnitude versus a strip waveguide MZI [87]. One would expect similar gains to be possible for photonic crystal waveguide sensors using a similar architecture.

5.6 Summary

A photonic crystal waveguide biosensor architecture has been presented. The bulk sensitivity of this sensor was shown to be 88 nm/RIU, similar to previously reported values. Specific biological detection was demonstrated using a biotin-streptavidin system. An improved sensing architecture with increased surface area in the high field region was demonstrated with a 40% increased bulk sensitivity.

6

Outlook: Towards Nonlinear Hybrid Photonic Crystal Architectures

6.1 Introduction

The concept of 'integrated optics' first appeared in the 1960s [88] as an analogue to integrated electronic circuits which were in rapid development at the time. The vision was of a dense array of active on-chip optical devices that would control light in the same manner as integrated circuits control electrical signals. Decades later, integrated optic systems remain of relatively low complexity and significantly greater size than comparable electronic systems [89].

Though the realization of an all-optical computer does not appear imminent, optical systems are still increasingly being incorporated into computer systems. Optical systems have been firmly entrenched in long distance data communication for many years. As the speed of microprocessors increases, 'long distance' communication shifts to shorter and shorter scales. Optical interconnects are already being used to communicate between CPUs in parallel computing applications and it has been proposed that optical interconnects will be implemented for signal transmission across a single die in the future.

Photonic crystals have emerged as a technology which stands to increase the functionality and decrease the size of integrated optical systems. By exploiting slow light modes of a dispersion engineered photonic crystal waveguide, silicon optical modulators with significantly reduced footprint size have been demonstrated [86].

Recently, Gu et al. demonstrated a gigahertz bandwidth photonic crystal waveguide modulator [87]. Using light with group velocity below 0.1c, they were able to reduce the interaction length of the interferometer by two orders of magnitude below that of milestone work using MOS capacitor silicon light modulation [90].

Silicon does not exhibit a strong optical nonlinearity, so existing demonstrations have rather relied on free-carrier dispersion. The high power consumption of this approach makes it unsuitable for dense on-chip applications [91]. Electro-optical refractive index modulation, on the other hand, is significantly faster and consumes far less power. To exploit the favourable characteristics of photonic crystals for application in creating compact interferometers, we present a hybrid approach, combining an electro-optically active film with a silicon photonic crystal waveguide.

6.1.1 Slow-light enhancement of optical modulators

Near the Brillouin zone boundary, the group velocity of the lowest frequency even mode of a silicon W1 photonic crystal goes to zero. This slow-light mode effectively compresses the optical signal and can be exploited to drastically enhance the phase sensitivity of small refractive index shift [27, 92, 93]. While it is possible to create slow light waveguides in other systems, photonic crystal waveguides also present the potential for slow light free of group-velocity dispersion, thereby optimizing the available bandwidth and preventing signal distortion [93, 94].

Modulators based on Mach-Zehnder interferometry consist of a single waveguide which splits into two branches, then recombines. Constructive or destructive interference at the output is accomplished by manipulating the relative output phase of the two waveguides. The phase difference between the two arms of the modulator is given by:

$$\Delta\phi = \frac{\omega}{c} nL \tag{6.1}$$

where ω is the angular frequency, c is the speed of light in vacuum, and n is the refractive index of the waveguide. The resulting transmitted output interference intensity is given by:

$$T = \frac{1}{2}(1 + cos(\Delta\phi)). \tag{6.2}$$

Restricting our examination to small variations of the index, the result is simply a parallel shift in the dispersion relation [93], given for frequency as:

$$\omega(k) \approx \omega_o(k) - \omega_s \sigma \frac{\delta n}{n} \tag{6.3}$$

where ω_s is the signal's carrier frequency, δn is the shift in the index, and σ is the portion of the energy in the affected material. In practice, the converse is usually considered, where the frequency of the incoming light is fixed and it is the wavevector which is altered, as in:

$$\Delta k(\omega_s) \approx -\frac{\omega_s \sigma \delta n}{n v_g} \tag{6.4}$$

and

$$\Delta\phi = \Delta k(\omega_s) L \tag{6.5}$$

where L is the length of the arm of the interferometer. In the case that a π radian phase shift is desired, the result is:

$$\frac{L}{\lambda_o} = \frac{1}{2\sigma} \frac{n}{\delta n} \frac{v_g}{c}. \tag{6.6}$$

The performance of such an interferometer can be improved by a factor of c/v_g by employing slow light [27]. The switching power required, either optical or electrical, will also be reduced by a factor of c/v_g.

6.1.2 Ionically self-assembled monolayer films

Poled-polymer organic second order nonlinear materials have been demonstrated for creating electro-optic modulators with $V_\pi < 1V$ [95] and with modulation rates greater than 150 GHz [96]. Their susceptibility to thermal and temporal relaxation, however, reduces their optical nonlinearity, impeding their implementation. Ionically self-assembled

monolayer films (ISAMs) have been presented as an alternative material system. ISAM films form a class of composite polyelectrolyte materials which can be created with high 2^{nd} order nonlinear coefficients [97]. ISAM films are fabricated by the sequential electrostatic binding of poly-anion and poly-cation layers (Figure 6.1). Electrostatically mediated binding ensures that each layer thickness is self-limiting such that a thick film can be formed with hundreds or thousands of individual monolayers.

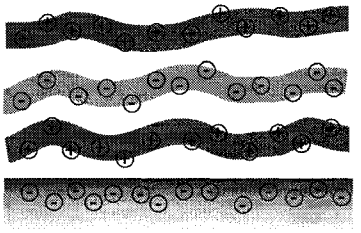

Figure 6.1: Successive ionically self-assembled monolayers are deposited to create an ISAM film.

The ISAM film technique can be used to create a noncentrosymmetric arrangement of chromophores resulting in a 2^{nd} order nonlinear film. The electro-optical properties of ISAMs do not tend to relax over time, and have been shown to be stable for a period of at least two years [97]. ISAM films are also relatively tolerant of heating and have been shown to fully recover their nonlinear optical properties after being heated to 150°C for 24 hours [98]. Their resilience to heating presents potential for direct patterning by imprint lithography, an attractive alternative to other expensive lithography techniques.

The ISAM film reported here is formed from a PCBS/PAH (poly 1-[4-(3-carboxy-4-hydroxyphenylazo) benzensulfonamido]-1,2-ethanediyl,sodium salt / poly(allylamine hydrochloride) bilayer structure which has an electro-optical coefficient r_{33} in the range of 1-2 pm/V. These films could be straightforwardly substituted with Procion Brown/PAH ISAM films which have been shown to have an electro-optic coefficients of $\approx$20 pm/V [99]. ISAM films used in this report were fabricated by Aruna Kroetch, using a process developed by Cemil Durak of the Randy Heflin group at Virginia Tech.

6.2 Hybrid photonic crystal architecture

One of the reasons for using silicon as a nanophotonic base material is its high refractive index (n≈3.5). Most ISAM films have a much lower refractive index (n≈1.6), making nanoscale optical confinement challenging. As an alternative to creating a purely ISAM photonic crystal structure, a hybrid Silicon/ISAM film structure has been devised. This hybrid stack combines a thin silicon photonic crystal layer with an ISAM film located within the field envelope to provide high optical nonlinearity (Figure 6.2).

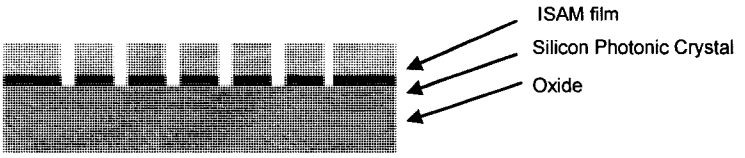

Figure 6.2: Conceptual approach to creating a hybrid ISAM/silicon photonic crystal structure (cross-section). A photonic crystal structure is patterned through an ISAM film into the underlying silicon layer.

For the hybrid structure to be effective, a balance must be found between photonic crystal confinement and containment of a significant fraction of the total optical power inside the nonlinear ISAM film. A 340 nm silicon slab as reported in Chapter 3 would tend to confine light within the silicon more tightly than desirable. By thinning the silicon film to 160 nm, the field power located in the ISAM film is predicted to be 18%, versus 5% for the 340 nm slab.

6.2.1 Modelling of hybrid photonic crystal

While photonic bandgaps have been demonstrated in low-index polymers [100], the bandgap for an ISAM film remains both narrower and at higher frequency than that of a silicon photonic crystal. Higher bandgap frequency makes out-plane confinement more challenging and while an air-clad ISAM planar photonic crystal could be well confined, an oxide substrate results in radiative losses. The hybrid ISAM/silicon structure avoids this issue as the bandgap is fully below the oxide light line (Figure 6.3).

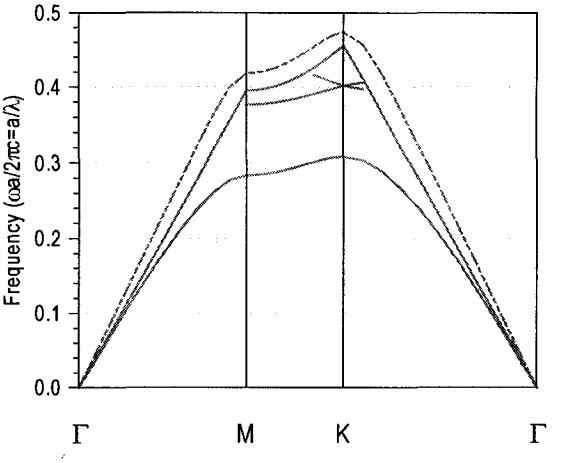

Figure 6.3: Band diagram for a hybrid ISAM/Silicon photonic crystal with thickness 0.3a and hole radius 0.35a. Solid gray line corresponds to oxide light line, dashed gray line corresponds to lowest order mode for the ISAM photonic crystal.

Although both the ISAM and silicon are patterned as photonic crystals in this approach, their bandgaps do not overlap and only the silicon layer behaves as a photonic crystal in the operating range.

6.3 Viability of photonic bandgap guidance in thin SOI

The hybrid silicon/ISAM film photonic crystal relies on photonic band-gap guidance of the thin silicon layer. To demonstrate that the thin silicon photonic crystal is capable of supporting photonic bandgap guidance, a thin 160 nm silicon slab was fabricated without the ISAM overcladding (Figure 6.4).

As in Chapter 4, the lowest order even mode cut-off of the waveguide was observed as evidence of photonic bandgap guidance. The observed transmission spectrum near the mode cut-off, seen in Figure 6.5, demonstrates the same characteristic behavior as photonic crystal waveguide fabricated in 340 nm SOI. Relative to a photonic crystal waveguide fabricated in a thicker slab, the transition from guidance to the bandgap is less abrupt, most likely due to the mode's reduced vertical confinement, making it more sensitive to scattering loss as the group index increases near the mode cut-off.

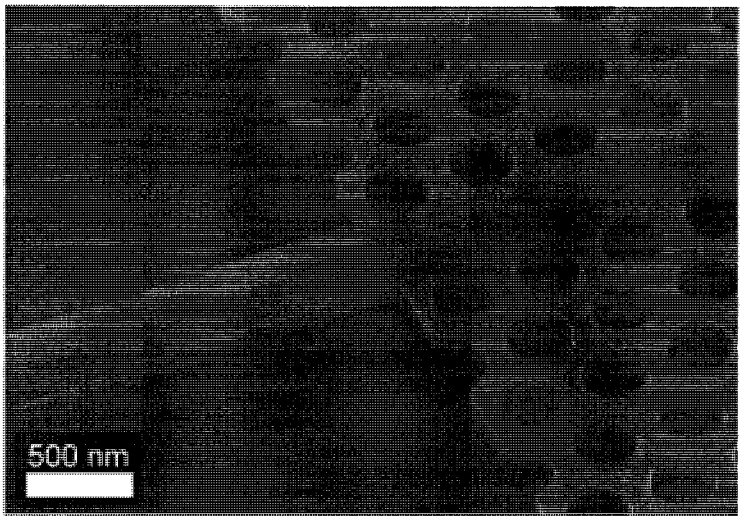

Figure 6.4: Interface between a silicon photonic crystal waveguide and strip waveguide patterned in a 160 nm silicon slab.

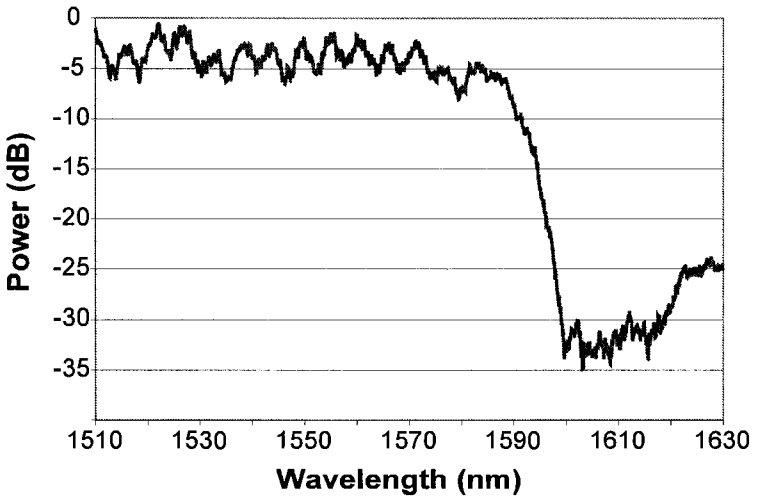

Figure 6.5: Photonic crystal waveguide guidance near the mode cut-off for 160 nm silicon slab. The transition is deeper but less abrupt than for the photonic crystals fabricated in a thicker slab.

6.4 Fabrication of hybrid silicon/ISAM film photonic crystals

Hybrid photonic crystal structures were fabricated by depositing an ISAM film on SOI, followed by lithographic patterning and a multi-stage etch to define the photonic crystal structure. Deposition and patterning of ISAM films was conducted in collaboration with colleague Aruna Kroetch.

In order that a significant fraction of the modal power lies within the ISAM film, the silicon slab thickness was reduced from 340 nm to 160 nm by progressive wet thermal oxidation at 800°C and oxide removal with an HF containing buffered oxide etch solution. The oxidization was performed at low temperature to slow the rate of silicon consumption and increase the controllability of the process. The rate of silicon consumed by oxidation at 800°C is plotted in Figure 6.6. A thin (≈20 nm) oxide layer was left unetched such that ISAM film growth could occur on the surface. It is likely that the thickness of this layer could be reduced dramatically with further testing.

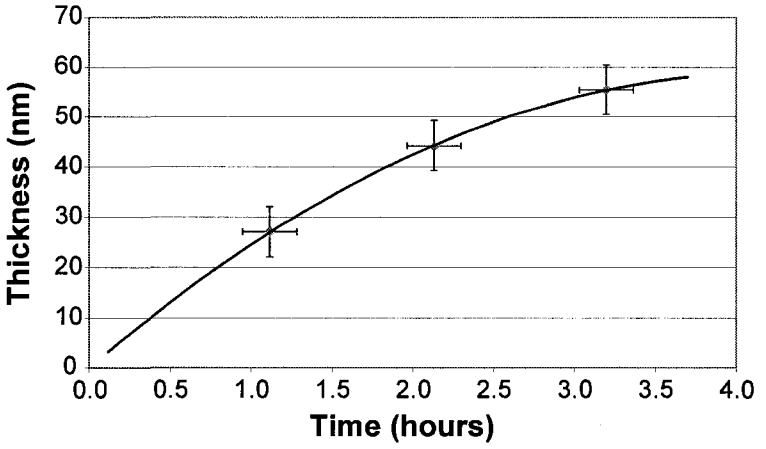

Figure 6.6: Silicon consumed by wet thermal oxidation at 800°C . Data points have been fitted with a second order polynomial.

The fabrication process, outlined in Figure 6.7, begins with a thinned SOI chip (a). Upon this chip a 240 bilayer ISAM film was then deposited (b). After baking to remove any absorbed moisture, a 580 nm layer of Shipley HPR 504 photoresist diluted 5:7 with ethyl lactate was spun over the ISAM film and baked at 115°C to drive off any remaining

solvent (c). The HPR 504 layer serves to protect the ISAM film as it would be rapidly attacked by the chrome etch solution. A 30 nm Cr masking layer was then deposited by sputter deposition with a Lesker magnetron sputtering system operated at a pressure of 2.5 mTorr with 300 W DC power (d). As outlined in Chapter 3, PMMA 950A2 was spun over the surface (e). After recalibrating the electron dose for a thinner silicon layer, electron beam lithography proceeded as before (f).

Following the development of the PMMA resist, the hybrid stack was etched in 4 stages:

1. After protecting the edges of the chip with HPR 504 (g), the Cr masking layer was etched in an ultrasonic Cr etch bath. Ultrasonic agitation was found to increase the homogeneity of the etching process (h).

2. The ISAM/HPR 504 layer was etched by an oxygen-plasma RIE with a oxygen flow of 15 sccm, an RF power of 60 W, and a chamber pressure of 5 mTorr (i).

3. The oxide layer was dry etched for 50 s using a CF_4 / CHF_3 RIE at 20 sccm and 30 sccm respectively with a chamber pressure of 100 mTorr and an RF power of 300 W (j).

4. Lastly, the silicon layer was dry etched for 40 s using the Cryo silicon etch recipe, detailed in Chapter 3 (k).

Following etching, the Cr masking layer can be removed by acetone lift-off of the HPR-504 (l). A hybrid stack strip waveguide created by this process prior to Cr removal can be seen in Figure 6.8. Photonic crystal waveguides (Figure 6.9) were successfully patterned in the silicon/ISAM stack.

Transmitted power was too low to demonstrate guidance, however. The high loss can be attributed to several factors. Roughness of both the etched sidewalls and inhomogeneities in the ISAM film are likely both contributing to make the photonic crystal much lossier than the silicon-only structure. As is, roughness from the Cr etch process and inhomogeneities from the ISAM film are reproduced in the underlying structure, imparting considerable sidewall roughness in the underlying silicon photonic crystal. It appears that this roughness has increased the loss in the waveguide to the point that the transmitted power is not

verifiably from the waveguide structure. It is expected that further improvements to the quality of the Cr etching and the ISAM film homogeneity would result in a functional hybrid Si/ISAM slab.

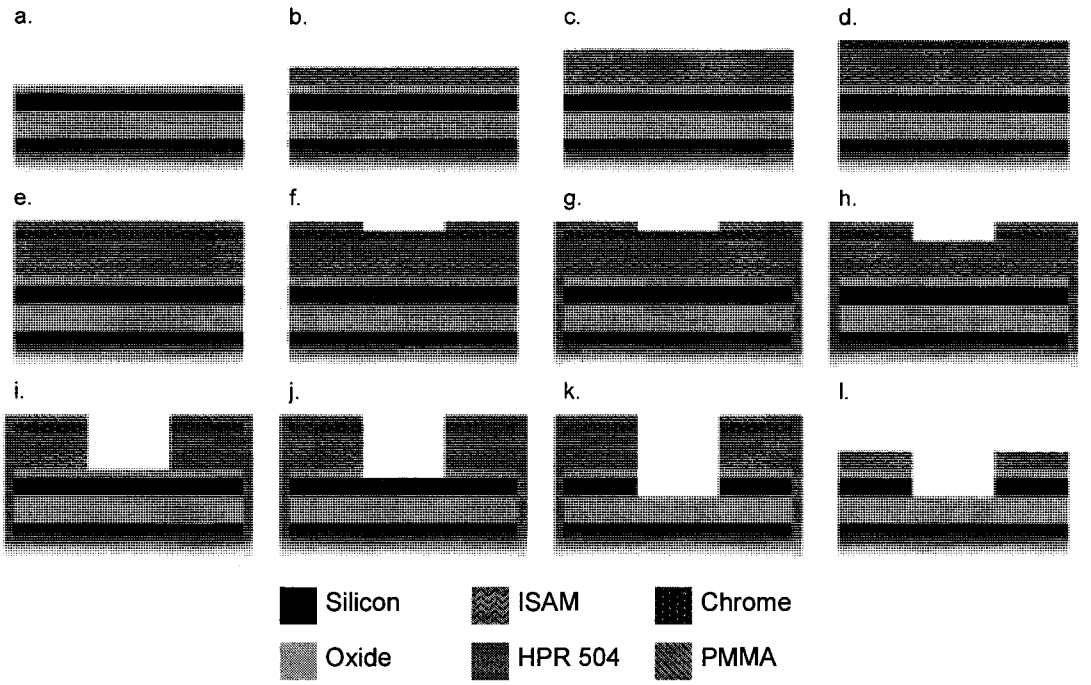

Figure 6.7: Summary of hybrid ISAM/Silicon photonic crystal fabrication process. (a) beginning with a thin SOI chip with a surface oxide, (b) deposit ISAM film, (c) spin on protective resist layer, (d) deposit chrome, (e) spin on resist, (f) pattern/develop resist, (g) coat edges with protective resist layer, (h) etch the chrome, (i) etch the resist and ISAM layer, (j) etch the oxide layer, (k) etch the silicon layer, and (l) strip the resist and remaining chrome.

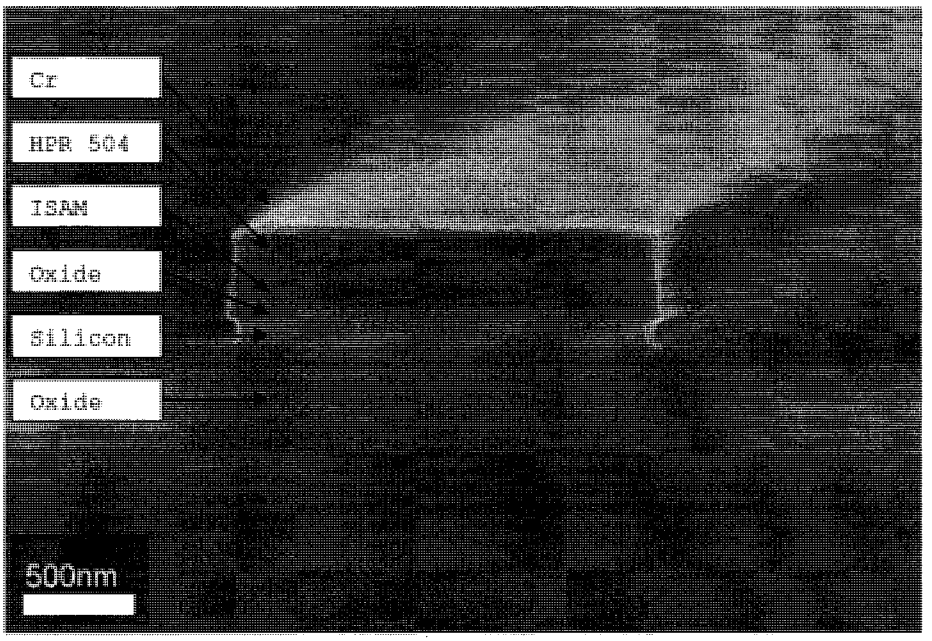

Figure 6.8: Strip waveguide demonstrating a fabricated hybrid silicon/ISAM stack.

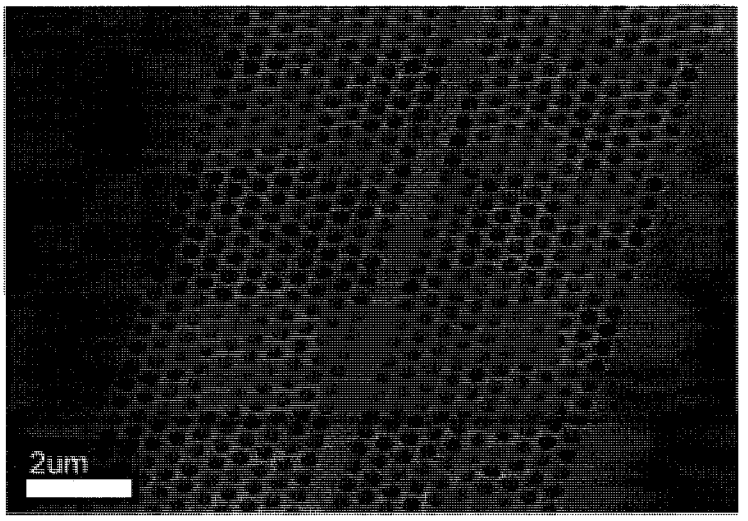

Figure 6.9: Photonic crystal waveguide patterned in a hybrid silicon/ISAM stack.

6.5 Summary

This chapter has detailed a fabrication procedure for incorporating an ISAM film with a silicon photonic crystal waveguide. This structure promises to combine the favourable electro-optical properties of an ISAM film with the novel dispersion characteristics of a planar silicon photonic crystal waveguide. While the hybrid Si/ISAM stack was successfully demonstrated and a photonic crystal was patterned, demonstration of photonic bandgap guidance was not observed due to the high loss of the waveguide. It is believed that the losses are due to roughness in the Cr and the ISAM film which are then transferred to the silicon photonic crystal.

7 Conclusion

7.1 Summary

This work has detailed the fabrication of silicon photonic crystals, demonstrated their potential for selective biosensing, and presented an architecture for the incorporation of a nonlinear polymer with planar photonic crystals.

Silicon photonic crystals were fabricated in SOI wafers using standard nanofabrication techniques. High resolution patterning was accomplished with electron beam lithography. Low-energy exposure reduces the penetration of the electron beam and was shown to be an acceptable alternative to proximity effect correction. Fixed beam writing was incorporated to significantly accelerate the patterning of less critical features, reducing the necessary exposure time. Silicon etching was demonstrated using two techniques, the 'Cryo' etch and the 'Unswitched' Bosch-like etch. Both were shown to yield acceptable results but the 'Unswitched' etch was found to be quicker and more reliable, at the expense of reduced selectivity to the resist mask.

The mode cut-off was detected to verify photonic bandgap guidance of patterned photonic crystal waveguides. The mode cut-off was shown to exist only for a single polarization and was shown to scale with the lattice dimension, as expected.

Photonic crystal waveguide biosensors of the type previously reported were demonstrated to have a bulk refractive index response of 88 nm/RIU. A thin MPMTS film with thickness of 5.6 nm was detected with a mode cut-off shift of 3.2 nm. A streptavidin film was detected as a 0.86 nm mode cut-off shift. The specificity of the streptavidin binding was verified with a negative control of pre -saturated streptavidin. A modified donor-defect photonic crystal waveguide architecture was demonstrated which was shown to have a bulk sensitivity of 120 nm/RIU, a 40% improvement over first generation design.

In order to combine the nonlinear properties of an ISAM film with a silicon photonic crystal structure, a hybrid fabrication approach was detailed. In this approach an ISAM film is deposited over a thin silicon photonic crystal, then a multilayer etch is performed to sequentially etch each species. The entire stack is patterned as a photonic crystal but the silicon layer is primarily responsible for confinement, with a portion of the evanescent field falling in the ISAM layer. The hybrid stack was successfully fabricated. However, the roughness transferred to silicon layer is significantly higher than in silicon-only structures and is believed to be causing increased losses such that the photonic crystal waveguiding was not observed.

Bibliography

[1] P. Vukusic and J. Sambles, "Photonic structures in biology," *Nature*, vol. 424, pp. 852–855, Aug. 2003.

[2] G. Tayeb, B. Gralak, and S. Enoch, "Structural colors in nature and butterfly-wing modeling," *Optics and Photonics News*, vol. 14, pp. 38–43, 2003.

[3] N. Ponnampalam and R. DeCorby, "Self assembled hollow waveguides with hybrid metal-dielectric bragg claddings," *Optics Express*, vol. 15, no. 20, 2007.

[4] J. Jewell, A. Scherer, S. McCall, Y. Lee, S. Walker, J. Harbison, and L. Florez, "Low-threshold electrically pumped vertical-cavity surface-emitting microlasers," *Electronics Letters*, vol. 25, no. 17, 1989.

[5] H. Sugawara, K. Itaya, H. Nozaki, and G. Hatakoshi, "High-brightness InGaAlP green light-emitting diodes," *Applied Physics Letters*, vol. 61, no. 15, 1992.

[6] J. Knight, "Photonic crystal fibers," *Nature*, vol. 424, pp. 847–851, 2003.

[7] T. Krauss, "Planar photonic crystal waveguide devices for integrated optics," *Physica Status Solidi (a)*, vol. 197, no. 3, pp. 668–702, 2003.

[8] O. Painter, A. Husain, A. Scherer, P. Lee, I. Kim, J. O'Brien, and P. Dapkus, "Lithographic tuning of a two-dimensional photonic crystal laser array," *IEEE Photonics Technology Letters*, vol. 12, no. 9, pp. 1126–1128, 2000.

[9] J. Strutt, "One the maintenance of vibrations by forces of double frequency and on the propagation of waves through a medium endowed with a periodic structure," *Philosophical Magazine*, vol. 24, no. 147, pp. 145–159, 1887.

[10] E. Yablonovitch, "Inhibited spontaneous emission in solid-state physics and electronics," *Physical Review Letters*, vol. 58, pp. 2059–2062, May 1987.

[11] S. John, "Strong localization of photons in certain disordered dielectric superlattices," *Physical Review Letters*, vol. 58, pp. 2486–2489, June 1987.

[12] E. Yablonovitch, T. Gmitter, and K. Leung, "Photonic band structure: the face-centered-cubic case employing nonspherical atoms," *Physical Review Letters*, vol. 67, pp. 2295–2298, Oct. 1991.

[13] U. Gruning, V. Lehmann, and C. Engelhardt, "Two-dimensional infrared photonic band gap structure based on porous silicon," *Applied Physics Letters*, vol. 66, pp. 3254–3256, June 1995.

[14] X. Xu, C. Hongda, and D. Zhang, "Enhancement of stimulated emission in 12-fold symmetric quasi-crystals," *Applied Physics B*, vol. 89, pp. 29–34, 2007.

[15] P. Lee, T. Lu, F. Tsai, and T. Lu, "Lasing actions of octagonal quasi-periodic photonic crystal microcavities," *Japanese Journal of Applied Physics*, vol. 46, no. 3A, pp. 971–973, 2007.

[16] N. Ashcroft and N. Mermin, *Solid state physics*. Philadelphia: Saunders College Publishing, 1976.

[17] M. Qui, "Effective index method for heterostructure-slab-waveguide-based two-dimensional photonic crystals," *Applied Physics Letters*, vol. 81, pp. 1163–1165, Aug. 2002.

[18] J. Joannopoulos, R. Mead, and J. Winn, *Photonic crystals: Molding the flow of light*. Princeton, NJ: Princeton Univ. Press, 2nd ed., 1995.

[19] K. Yee, "Numerical solution of initial boundary value problems involving maxwell's equations," *IEEE Tran. Antennas Propag.*, vol. 14, pp. 302–307, May 1966.

[20] T. Krauss, R. DeLaRue, and S. Brand, "Two-dimensional photonic bandgap structures operating at near infrared wavelengths," *Nature*, vol. 383, pp. 699–702, Oct. 1996.

[21] S. Noda, M. Imada, A. Chutinan, and N. Yamamoto, "III-V based-semiconductor photonic crystals," *Optical and Quantum Electronics*, vol. 34, pp. 723–736, 2002.

[22] D. Atkin, P. Russel, T. Birks, and P. Roberts, "Photonic band structure of guided Bloch modes in high index films fully etched through with periodic microstructure," *Journal of Modern Optics*, vol. 43, no. 5, pp. 1035–1053, 1996.

[23] E. Yablonovitch, T. Gmitter, R. Meade, A. Rappe, K. Brommer, and J. Joannopoulos, "Donor and acceptor modes in photonic band structure," *Physical Review Letters*, vol. 67, no. 24, pp. 3380–3383, 1991.

[24] A. Mekis, A. Chen, I. Kurland, S. Fan, P. Villeneuve, and J. Joannopoulos, "High transmission through sharp bends in photonic crystal waveguides," *Physical Review Letters*, vol. 77, no. 18, p. 77, 1996.

[25] M. Tokushima, H. Kosaka, A. Tomita, and H. Yamada, "Lightwave propagation through a 120° sharply bent single-line-defect photonic crystal waveguide," *Applied Physics Letters*, vol. 76, no. 8, pp. 952–954, 2000.

[26] A. Petrov and M. Eich, "Zero dispersion at small group velocities in photonic crystal waveguides," *Applied Physics Letters*, vol. 85, no. 21, pp. 4866–4868, 2004.

[27] M. Soljacic, S. Johnson, S. Fan, M. Ibanescu, E. Ippen, and J. Joannopoulos, "Photonic crystal enhancement of nonlinear phase sensitivity," *J. Opt. Soc. Am.*, vol. 19, no. 9, pp. 2052–2059, 2002.

[28] R. Meade, A. Devenyl, J. Joannopoulos, O. Alerhand, D. Smith, and K. Kash, "Novel applications of photonic band gap materials: Low-loss bends and high-Q cavities," *Journal of Applied Physics*, vol. 75, no. 9, pp. 4753–4755, 1994.

[29] M. Bruel, B. Aspar, B. Charlet, C. Maleville, T. Poumeyrol, A. Soubie, H. Auberton-Herve, J. Lamure, T. Barge, F. Metral, and S. Trucchi, "Smart-cut: a promising new SOI material technology," *SOI Conference 1995, IEEE International*, pp. 178–179, 1995.

[30] T. Arentoft, J. Sondergaard, M. Kristensen, A. Boltasseva, M. Thorhauge, and L. Frandsen, "Low-loss silicon-on-insulator photonic crystal waveguides," *Electronics Letters*, vol. 38, no. 6, pp. 274–275, 2002.

[31] W. Bogaerts, R. Baets, P. Dumon, V. Wiaux, S. Beckx, D. Taillaert, B. Luyssaert, and D. Thourhout, "Nanophotonic waveguides in silicon on insulator fabricated with CMOS technology," *Journal of Lightwave Technology*, vol. 23, pp. 401–412, Jan 2005.

[32] R. Wuest, F. Robin, C. Hunziker, and P. Strasser, "Limitations of proximity effect corrections for electron-beam patterning of planar photonic crystals," *Optical Engineering*, vol. 44, no. 4, 2005.

[33] B. Houli, V. Umansky, and M. Heiblum, "Low energy electron beam lithography with 30 nm resolution," *Semiconductor Science and Technology*, vol. 8, pp. 1490–1492, 1993.

[34] D. Drouin, A. Couture, X. Tastet, V. Aimez, and R. Gauvin, "Casino v2.42 - a fast and easy-to-use modeling tool for scannning electron microscopy and microanalysis users," *Scanning*, vol. 29, no. 3, pp. 92–101, 2007.

[35] K. Tachi, S. Tsujimoto, and Okudaira, "Low temperature reactive ion etching and microwave plasma etching of silicon," *Applied Physics Letters*, vol. 52, pp. 616–618, 1988.

[36] M. deBoer, J. Gardeniers, H. Jansen, E. Smulders, M. Gilde, G. Roelofs, J. Sasserath, and M. Elwenspoek, "Guidelines for etching silicon MEMS structures using fluorine high-density plasmas at cryogenic temperatures," *Journal of Microelectromechanical Systems*, vol. 11, Aug. 2002.

[37] C. Welch, A. Goodyear, G. Ditmer, and G. Tan, "Choice of silicon etch processes for opto- and microelectronic device fabrications using inductively coupled plasmas," *Optoelectronic and Microelectronic Materials and Devices, 2004 Conference on*, pp. 13–16, 2004.

[38] F. Laermer and A. Schilp, "Method of anisotropically etching silicon," *US Patent No. 5501893*, 1996.

[39] T. Baba, N. Fukaya, and J. Yonekura, "Observation of light propagation in photonic crystal optical waveguides with bends," *Electronics Letters*, vol. 35, no. 8, pp. 654–655, 1999.

[40] L. Clark and J. Lions, "Electrode systems for continuous monitoring in cardiovascular surgery," *Annals of the New York Academy of Science*, vol. 102, no. 29, 1962.

[41] D. Erickson, S. Mandal, A. Yang, and B. Bordovez, "Nanobiosensors: optofluidic, electrical, and mechanical approaches to biomolecular detection at the nanoscale," *Microfluid Nanofluid*, vol. 4, pp. 33–52, 2008.

[42] P. Lu, "Early detection of avian influenza," *Science*, vol. 312, no. 5772, p. 337, 2006.

[43] T. Straub and D. Chandler, "Towards a unified system for detecting waterborne pathogens," *Journal of Microbiological Methods*, vol. 53, no. 2, pp. 185–197, 2003.

[44] A. Rasooly and K. Herold, "Biosensors for the analysis of food- and waterborne pathogens and their toxins," *Journal of AOAC International*, vol. 89, no. 3, pp. 873–883, 2004.

[45] L. Stetzenbach, M. Buttner, and P. Cruz, "Detection and enumeration of airborne biocontaminants," *Current Opinion in Biotechnology*, vol. 15, no. 3, pp. 185–197, 2004.

[46] J. Growdon, "Biomarkers of alzheimer disease," *Archives of Neurology*, vol. 56, no. 3, pp. 281–283, 1999.

[47] C. Sander, "Genomic medicine and the future of health care," *Science*, vol. 287, no. 5460, pp. 4854–4856, 2000.

[48] P. Srinivas, M. Verma, Y. Zhao, and S. Srivastava, "Proteomics for cancer biomarker discovery," *Clinical Chemistry*, vol. 48, no. 8, pp. 1160–1169, 2002.

[49] J. Ross, D. Schenkein, O. Kahala, G. Linette, J. Stec, W. Symmans, L. Pusztai, and G. Hortobagyi, "Pharmacogenomics," *Advances in Anatomic Pathology*, vol. 11, no. 4, pp. 211–220, 2004.

[50] T. Vo-Dinh and L. Allain, *Biomedical Photonics Handbook*, ch. Biosensors for Medical Applications. Boca Raton: CRC Press LLC, 1st ed., 2003.

[51] K. Marx, "Quartz crystal microbalance: a useful tool for studying thin polymer films and complex biomolecular systems at the solution-surface interface," *Biomacromolecules*, vol. 4, no. 5, pp. 1099–1120, 2003.

[52] H. Zhang and E. Kim, "Micromachined acoustic resonant mass sensor," *Journal of Microelectromechanical Systems*, vol. 14, no. 4, pp. 699–706, 2005.

[53] R. Lucklum and P. Hauptmann, "Acoustic microsensors - the challenge behind microgravimetry," *Analytical Bioanalytical Chemistry*, vol. 384, no. 3, pp. 667–682, 2006.

[54] B. Ilic, Y. Yang, K. Aubin, R. Reichenbach, S. Krylov, and H. Craighead, "Enumeration of DNA molecules bound to a nanomechanical oscillator," *Nano Letters*, vol. 5, no. 5, pp. 925–929, 2005.

[55] B. Ilic, D. Czaplewski, M. Zalalutdinov, H. Craighead, P. Neuzil, C. Campagnolo, and C. Batt, "Single cell detection with micro-mechanical oscillators," *Journal of Vacuum Science Technology B*, vol. 19, no. 6, pp. 2825–2828, 2001.

[56] A. Gupta, P. Nair, D. Akin, M. Ladisch, S. Broyles, M. Alam, and R. Bashir, "Anomalous resonance in a nanomechanical biosensor," *Proceedings of the National Academy of Science USA*, vol. 103, no. 36, pp. 13362–13367, 2006.

[57] Y. Yang, C. Callegari, X. Feng, K. Ekinci, and M. Roukes, "Zeoptogram-scale nanomechanical mass sensing," *Nano Letters*, vol. 6, no. 4, pp. 583–586, 2006.

[58] K. Ataka and J. Heberle, "Biochemical applications of surface-enhanced infrared absorption spectroscopy," *Analytical Bioanalytical Chemistry*, vol. 388, pp. 47–54, 2007.

[59] M. Ramanathan and A. Simonian, "Array biosensor based on enzyme kinetics monitoring by fluorescence spectroscopy: application for neurotoxins detection," *Biosensors and Bioelectronics*, vol. 22, pp. 3001–3007, 2007.

[60] D. Papkovski, T. Oriordan, and A. Soini, "Phosphorescent porphyrin probes in biosensors and sensitive bioassays," *Biochemical Society Transactions*, vol. 28, pp. 74–77, 2000.

[61] E. Schipper, R. Kooyman, A. Borreman, and J. Greve, "The critical sensor: a new type of evanescent wave immunosensor," *Biosensors and Bioelectronics*, vol. 11, no. 3, pp. 295–304, 1995.

[62] I. Notingher, J. Selvakumaran, and L. Hench, "New detection system for toxic agents based on continuous spectroscopic monitoring of living cells," *Biosensors and Bioelectronics*, vol. 20, no. 4, pp. 780–789, 2004.

[63] C. Haynes, C. Yonzon, X. Zhang, and R. Van Duyne, "Surface-enhanced raman sensors: early history and the development of sensors for quantitative biowarfare agent and glucose detection," *Journal of Raman Spectroscopy*, vol. 36, pp. 471–484, 2005.

[64] M. Lee and P. Fauchet, "Two-dimensional silicon photonic crystal based biosensing platform for protein detection," *Optics Express*, vol. 15, pp. 4530–4535, 2007.

[65] N. Skivesen, A. Ttu, M. Kristensen, J. Kjems, L. Frandsen, and P. Borel, "Photonic-crystal waveguide biosensor," *Optics Express*, vol. 15, pp. 3169–3176, 2007.

[66] P. Lambeck, "Integrated optical sensors for the chemical domain," *Measurement Science and Technology*, vol. 17, Aug. 2006.

[67] O. Levi, M. Lee, J. Zhang, V. Lousse, S. Brueck, S. Fan, and J. Harris, "Sensitivity analysis of a photonic crystal structure for index-of-refraction sensing," *Proceedings of SPIE*, vol. 6447, 2007.

[68] J. Jensen, P. Hoiby, G. Emiliyanov, O. Bang, L. Pedersen, and A. Bjarklev, "Selective detection of antibodies in microstructured polymer optical fibers," *Optics Express*, vol. 13, no. 15, pp. 5883–5889, 2005.

[69] L. Rindorf, J. Jensen, M. Dufva, L. Pedersen, P. Hoiby, and O. Bang, "Photonic crystal fiber long-period gratings for biochemical sensing," *Optics Express*, vol. 14, no. 18, pp. 8224–8231, 2006.

[70] L. Stefano, L. Rotiroti, I. Rendina, L. Moretti, V. Scognamiglio, M. Rossi, and S. D'Auria, "Porous silcon-based optical microsensor for the detection of l-glutamine," *Biosensors and Bioelectronics*, vol. 21, no. 8, pp. 1664–1667, 2006.

[71] O. Meskini, A. Abdelghani, A. Tlili, R. Mgaieth, N. Jaffrezic-Renault, and C. Martelet, "Porous silicon as functionalized material for immunosensor application," *Talanta*, vol. 3, pp. 1430–1433, 2007.

[72] M. Lee and P. Fauchet, "Two-dimensional Si photonic crystal microcavity for single particle detection," *Group IV Photonics, 2007 4th IEEE International Conference on*, pp. 1–3, Sept 2007.

[73] L. Mirkarimi, S. Zlatanovic, S. Sigalas, M. Bynum, K. Robotti, E. Chow, and A. Grot, "Toward single molecule detection with photonic crystal microcavity biosensors," *LEOS Summer Tropical Meetings, 2006 Digest of the*, pp. 29–30, July 2006.

[74] E. Chow, A. Grot, L. Mirkarimi, M. Sigalas, and G. Girolami, "Ultra-compact biochemical sensor built with two dimensional photonic crystal microcavity," *Quantum Electronics Conference, 2004. (IQEC) International,*, pp. 788–789, 2004.

[75] E. Chow, A. Grot, L. W. Mirkarimi, M. Sigalas, and G. Girolami, "Ultracompact biochemical sensor built with two-dimensional photonic crystal microcavity," *Optics Letters*, vol. 29, no. 10, pp. 1093–1095, 2004.

[76] M. Lee and P. Fauchet, "Nanoscale microcavity sensor for single particle detection," *Optics Letters*, vol. 32, pp. 3284–3286, 2007.

[77] D. Erickson, T. Rockwood, T. Emery, A. Scherer, and D. Psaltis, "Nanofluidic tuning of photonic crystal circuits," *Optics Letters*, vol. 31, pp. 59–61, 2006.

[78] J. Topolancik, P. Bhattacharya, J. Sabarinathan, and P. Yu, "Fluid detection with photonic crystal-based multi channel waveguides," *Applied Physics Letters*, vol. 82, pp. 1143–1145, 2003.

[79] R. Ferrini, J. Martz, L. Zuppiroli, B. Wild, V. Zabelin, L. Dunbar, R. Houdre, M. Mulot, and S. Anand, "Planar photonic crystals infiltrated with liquid crystals: optical characterization of molecule orientation," *Optics Letters*, vol. 31, pp. 1238–1240, 2006.

[80] J. Homola, S. Yee, and G. Gauglitz, "Surface plasmon resonance sensors: review," *Sensors and Actuators B*, vol. 54, pp. 3–15, 1999.

[81] F. Hook, J. Vorors, M. Rodahl, R. Kurrat, P. Boni, J. Ramsden, M. Textor, N. Spencer, P. Tengvall, J. Gold, and B. Kasemo, "A comparative study of protein adsorption on titanium oxide surfaces using in situ ellipsometry, optical waveguide ligthmode spectroscopy, and quartz crystal microbalance/dissipation," *Colloids and Surfaces B*, vol. 24, pp. 155–170, 2002.

[82] Y. Tanaka, T. Asano, R. Hatsuta, and S. Noda, "Analysis of a line-defect waveguide on a silicon-on-insulator two-dimensional photonic crystal slab," *Journal of Lightwave Technology*, vol. 22, no. 12, 2004.

[83] Y. Tanaka, T. Asano, Y. Akahane, B. Song, and S. Noda, "Theoretical investigation of a two-dimensional photonic crystal slab with truncated cone air holes," *Applied Physics Letters*, vol. 82, no. 11, 2003.

[84] "(3-mercaptopropyl)trimethoxysilane: Refractive index." Data Sheet, Sigma Aldrich Inc. 2008.

[85] R. Heideman and P. Lambeck, "Remote opto-chemical sensing with extreme sensitivity: design, fabrication and performance of a pigtailed integrated optical phase-modulated Mach-Zehnder interferometer system," *Sensors and Actuators B*, vol. 61, p. 100, 1999.

[86] Y. Vlasov, M. O'Boyle, H. Hamann, and S. McNab, "Active control of slow light on a chip with photonic crystal waveguides," *Nature*, vol. 3, pp. 65–69, 2005.

[87] L. Gu, W. Jiang, X. Chen, L. Wang, and R. Chen, "High speed silicon photonic crystal waveguide modulator for low voltage operation," *Applied Physics Letters*, vol. 90, no. 071105, 2007.

[88] S. Miller, "Integrated optics - an introduction," *Bell System Technical Journal*, vol. 48, pp. 2059–2069, 1969.

[89] L. Thylen, M. Qui, and S. Anand, "Photonic crystals - a step toward integrated circuits for photonics," *ChemPhysChem*, vol. 5, pp. 1268–1283, 2004.

[90] P. Dainesi, A. Kung, M. Chabloz, A. Lagos, P. Fluckiger, A. Ionescu, P. Fazan, M. Declerq, P. Renaud, and P. Robert, "CMOS compatible fully integrated mach-zehnder interferometer in SOI technology," *Photonics Technology Letters*, vol. 12, no. 6, pp. 660–662, 2000.

[91] D. Miller, "Rational and challenges for optical interconnects to electronic chips," *Proceedings of the IEEE*, vol. 88, pp. 728–749, June 2000.

[92] Z. Shi, R. Boyd, D. Guathier, and C. Dudley, "Enhancing the spectral sensitivity of interferometers using slow-light media," *Optics Letters*, vol. 32, no. 8, 2007.

[93] M. Soljacic and J. Joannopoulos, "Enhancement of nonlinear effects using photonic crystals," *Nature*, vol. 3, pp. 211–219, 2004.

[94] M. Settle, R. Engelen, M. Salib, A. Michaeli, L. Kuipers, and T. Krauss, "Flatband slow light in photonic crystals featuring spatial pulse compression and terahertz bandwidth," *Optics Express*, vol. 15, no. 1, 2007.

[95] Y. Shi, C. Zhang, J. Bechtel, L. Dalton, B. Robinson, and W. Steier, "Low (sub-1-volt) halfwave voltage polymeric electro-optic modulators achieved by controlling chromophore shape," *Science*, vol. 288, pp. 119–122, 2000.

[96] M. Lee, H. Katz, C. Erben, D. Gill, J. Gopalan, and D. McGee, "Broadband modulation of light by using an electro-optic polymer," *Science*, vol. 298, pp. 1401–1403, 2002.

[97] J. Heflin, C. Durak, P. Neyman, C. Brands, M. Guzy, K. Gaskins, A. Garg, R. Davis, and K. Van Cott, "Organic electro-optic films fabricated by hybrid covalent/ionic self-assembly," *Lasers and Electro-optics, 2005 (CLEO). Conference on,*, vol. 3, pp. 1864–1866, May 2005.

[98] J. Heflin, M. Guzy, P. Neyman, K. Gaskins, C. Brands, Z. Wang, R. Gibson, H.W. anad Davis, and K. Van Cott, "Efficient, thermally stable second order nonlinear optical response in organic hybrid covalent/ionic self assembled films," *Langmuir*, vol. 22, pp. 5723–5727, 2006.

[99] J. Heflin, Y. Liu, C. Figura, D. Marciu, and R. Claus, "Second order nonlinear optical thin films fabricated from ionically self-assembled monolayers," *Proceedings of SPIE*, vol. 3147, pp. 10–19, 1997.

[100] U. Hubner, R. Boucher, F. Marlow, and W. Volksen, "Omnidirectional photonic band gap in polymer photonic crystal slabs," *Applied Physics Letters*, vol. 91, no. 22, 2007.